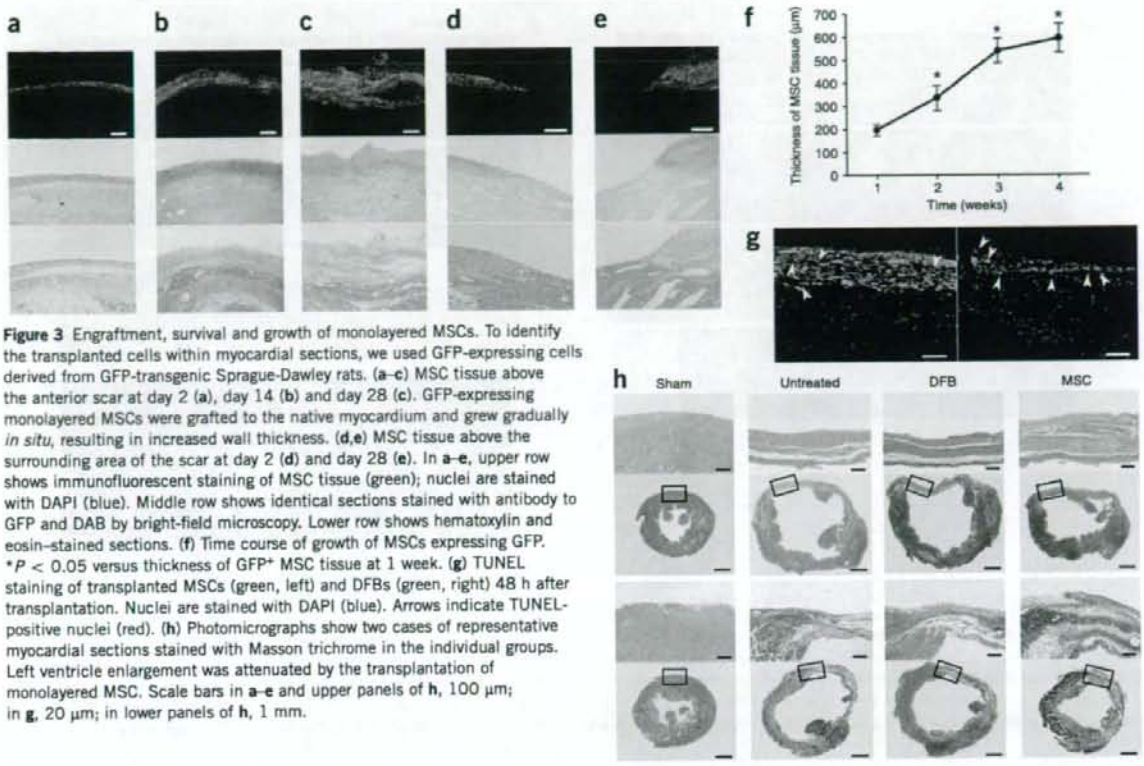

Figure 3 Engraftment, survival and growth of monolayered MSCs. To identify the transplanted cells within myocardial sections, we used GFP-expressing cells derived from GFP-transgenic Sprague-Dawley rats. (**a**–**c**) MSC tissue above the anterior scar at day 2 (**a**), day 14 (**b**) and day 28 (**c**). GFP-expressing monolayered MSCs were grafted to the native myocardium and grew gradually *in situ*, resulting in increased wall thickness. (**d**,**e**) MSC tissue above the surrounding area of the scar at day 2 (**d**) and day 28 (**e**). In **a**–**e**, upper row shows immunofluorescent staining of MSC tissue (green); nuclei are stained with DAPI (blue). Middle row shows identical sections stained with antibody to GFP and DAB by bright-field microscopy. Lower row shows hematoxylin and eosin–stained sections. (**f**) Time course of growth of MSCs expressing GFP. $^*P < 0.05$ versus thickness of GFP$^+$ MSC tissue at 1 week. (**g**) TUNEL staining of transplanted MSCs (green, left) and DFBs (green, right) 48 h after transplantation. Nuclei are stained with DAPI (blue). Arrows indicate TUNEL-positive nuclei (red). (**h**) Photomicrographs show two cases of representative myocardial sections stained with Masson trichrome in the individual groups. Left ventricle enlargement was attenuated by the transplantation of monolayered MSC. Scale bars in **a**–**e** and upper panels of **h**, 100 μm; in **g**, 20 μm; in lower panels of **h**, 1 mm.

rejection. Using flow cytometry, we did not find any substantial differences between adipose tissue–derived MSCs and bone marrow–derived MSCs, consistent with results from previous studies[22,25]. Adipose-derived MSCs readily attached to and propagated on the temperature-responsive dish. Abdominal subcutaneous adipose tissue is clinically redundant and easily accessible by rapid and minimally invasive surgery such as liposuction. Thus, adipose tissue may serve as a source of stem cells for therapeutic cell sheets.

Here, monolayered MSCs could readily be transferred and grafted to the scarred myocardium without additives or suturing. This may be attributable to cell-to-cell connections as well as extracellular matrix deposits on the basal surface of the monolayered MSCs. Regeneration of myocardial mass is thought to require multilayered constructs of the cell sheet. Unfortunately, however, the lack of a vascular network has limited the formation of a thick construct[10,29]. The transplanted monolayered MSCs thickened gradually, developing into a stratum of up to 600 μm in thickness over the native tissue 4 weeks after transplantation, suggesting that monolayered MSCs have an ability to grow *in situ*. As a result, the transplanted MSC tissue reversed wall thinning of the infarcted myocardium. On the other hand, the fibroblast sheet did not grow *in situ*. It should be noted that the MSC tissue included a large number of newly formed blood vessels. These vessels were composed of graft-derived cells, host-derived cells or both. The MSC sheet secreted a large amount of angiogenic and antiapoptotic cytokines, including VEGF and HGF, as compared with the fibroblast sheet. These results suggest that MSCs induce neovascularization within the sheet not only through their ability to differentiate into vascular cells but also through growth factor–mediated paracrine regulation. Thus, we believe that the angiogenic action of MSCs is important for reconstruction of cardiac mass by the MSC tissue.

Four weeks after transplantation, a small fraction of the engrafted MSCs were positive for cardiac proteins such as cardiac troponin T and desmin, suggesting the presence of cardiomyocytes within the MSC tissue. FISH analysis suggested that the most cardiomyocytes within the MSC tissue were not derived from cell fusion, but we are unable to exclude the possibility that some were. Further studies are necessary to investigate the mechanisms by which MSCs within the MSC tissue regenerate cardiomyocytes. The majority of the MSC tissue was positive for vimentin, a marker for undifferentiated MSCs and fibroblasts. In addition, the majority of MSCs within the graft were negative for collagen type I and αSMA, a marker for myofibroblasts. These results suggest that the grown-up MSC tissue is composed of newly formed blood vessels, undifferentiated MSCs and few cardiomyocytes.

We have also shown that transplantation of the monolayered MSCs significantly increased left ventricle maximum dP/dt, decreased LVEDP and inhibited the development of left ventricle enlargement in rats with chronic heart failure secondary to myocardial infarction. These results suggest that transplantation of monolayered MSCs improves cardiac function. But the presence of cardiomyocytes within the MSC tissue seemed to be rare. Thus, this improvement may be explained mainly by growth factor–mediated paracrine effects of the MSC sheet and a decrease in left ventricle wall stress resulting from the thick MSC tissue. Furthermore, no rats treated with the monolayered MSCs died during the study period, although untreated rats died frequently. These results indicate that fatal arrythmogenic problems were not caused by integration of the MSC tissue.

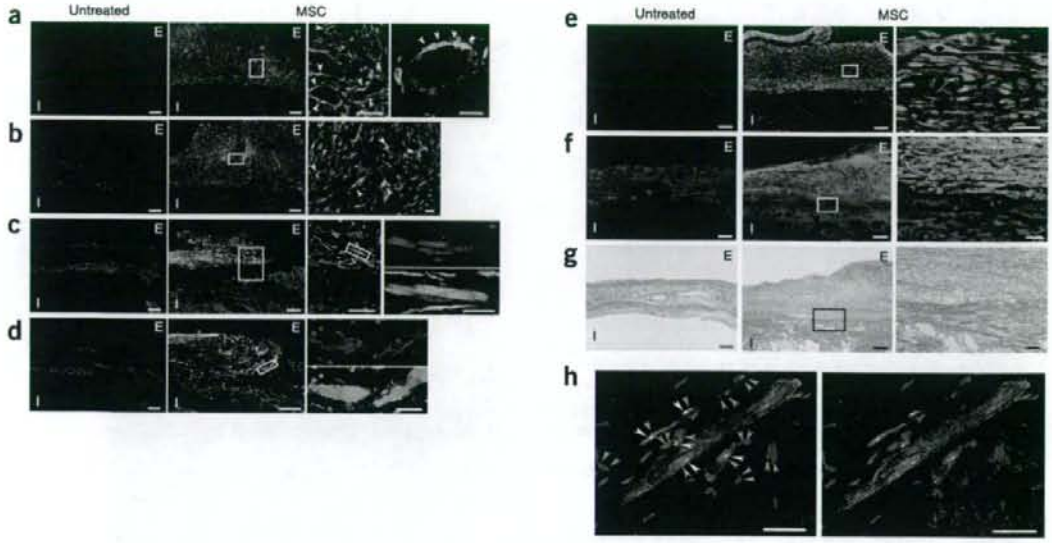

Figure 4 Differentiation of MSCs within the MSC tissue after growth *in situ*. (**a**,**b**) GFP-expressing MSCs (green) were identified as a thick stratum at the epicardial side of the myocardium. The MSC tissue contained a number of vascular structures positive for vWF (red, **a**) and αSMA (red, **b**). MSCs that did not participate in blood vessel formation were only rarely positive for αSMA, a marker for myofibroblasts. Arrows indicate transplanted MSCs positive for vWF or αSMA. (**c**,**d**) Some MSCs within the MSC tissue were positive for cardiac markers cardiac troponin T (red, **c**) and desmin (red, **d**). (**e**) Most of the MSC tissue was positive for vimentin (red). (**f**) The MSC tissue modestly stained for collagen type 1 (red). (**g**) Collagen deposition was also detected by picrosirius red staining. (**h**) FISH analysis. Newly formed cardiomyocytes (desmin, red) that were positive for GFP (green) had only one set of X (purple) and Y chromosomes (white), whereas two X chromosomes were detected exclusively in GFP^- host-derived cells. Nuclei are stained with DAPI (blue, **a**–**f** and **h**). Scale bars in left three panels of **a** and **c** and in two left panels of **b** and **d**–**g**, 100 μm; in **h** and far right panels of **a**–**g**, 20 μm. E, epicardial side; I, intimal side.

In summary, adipose tissue–derived monolayered MSCs can be readily engrafted to the scarred myocardium, grow gradually *in situ* and become a thick stratum that includes newly formed vessels, cardiomyocytes and undifferentiated MSCs. The engrafted MSCs reversed wall thinning in the scar area and improved cardiac function and survival in rats with myocardial infarction. Thus, transplantation of monolayered MSCs may be a new therapeutic strategy for cardiac tissue regeneration.

METHODS

Model of heart failure. All protocols were performed in accordance with the guidelines of the Animal Care Ethics Committee of the Japanese National Cardiovascular Center Research Institute. We used male Sprague-Dawley rats (Japan SLC) weighing 187–215 g. A myocardial infarction model was produced by ligation of the left coronary artery, as described previously[30]. Briefly, we anesthetized rats with sodium pentobarbital (30 mg/kg) and ventilated them with a volume-regulated respirator. We exposed hearts by left thoracotomy, and ligated the left coronary artery 2–3 mm from its origin between the pulmonary artery conus and the left atrium with a 6-0 Prolene suture. The sham group underwent thoracotomy and cardiac exposure without coronary ligation. The surviving rats were maintained on standard rat chow.

Study protocol. We randomly placed rats into four groups: rats with chronic heart failure that underwent transplantation of monolayered MSCs (MSC group; $n = 12$), rats with chronic heart failure given monolayered DFBs (DFB group; $n = 12$), rats with chronic heart failure without transplantation (untreated group; $n = 12$) and sham-operated rats without transplantation (sham group; $n = 10$). Four weeks after coronary ligation, the MSC and DFB groups underwent autologous transplantation of each monolayered cell graft onto the anterior wall, including the scar area (**Supplementary Methods** online). The other two groups underwent the same operative procedures without transplantation. We performed hemodynamic studies, echocardiography and histological assessments 4 and 8 weeks after coronary ligation (**Supplementary Methods**). Upon killing at 8 weeks after coronary ligation, only those rats with infarct size >25% of the left ventricle area were included in this study. Therefore, the variation in infarct size between the experimental rats was relatively low (28–41%, average 33.9% ± 1.9%).

Isolation and culture of MSCs from adipose tissue. Immediately after coronary ligation, we acquired subcutaneous adipose tissue (1.1 ± 0.1 g) from the right inguinal region of each rat. We minced adipose tissue with scissors and digested it with 10 ml of type 1 collagenase solution (0.1 mg/ml, Worthington Biochemical) for 1 h in a 37 °C water bath shaker. After filtration with mesh filter (Costar 3480, Corning) and centrifugation at 780*g* for 8 min, we suspended isolated cells in α-MEM supplemented with 10% FCS and antibiotics, plated them onto a 100-mm dish and incubated them at 37 °C with 5% CO_2. A small number of spindle-shaped cells were apparent in visible symmetric colonies by days 5–7.

Preparation of temperature-responsive dishes. Specific procedures for preparation of square-designed PIPAAm-grafted dishes have been previously described[9]. Briefly, we spread IPAAm monomer (Kohjin) in 2-propanol solution onto 60-mm polystyrene culture dishes (Corning). We then subjected the dishes to irradiation (0.25-MGy electron beam dose) using an Area Beam Electron Processing system (Nisshin High-Voltage) to immobilize IPAAm on the dish surface; we then rinsed dishes with cold distilled water and dried them in nitrogen gas. In the second step, we masked the PIPAAm-grafted surface with a square glass coverslip (24 × 24 mm, Matsunami Glass). We spread acrylamide (AAm) monomer solution in 2-propanol onto the masked dish surface. We then irradiated the dish surface with an electron beam and washed it. As a result, the central square area of each dish was PIPAAm grafted (temperature responsive), and the surrounding border was poly-AAm grafted (non–cell adhesive). This PIPAAm-grafted surface is hydrophobic under culture

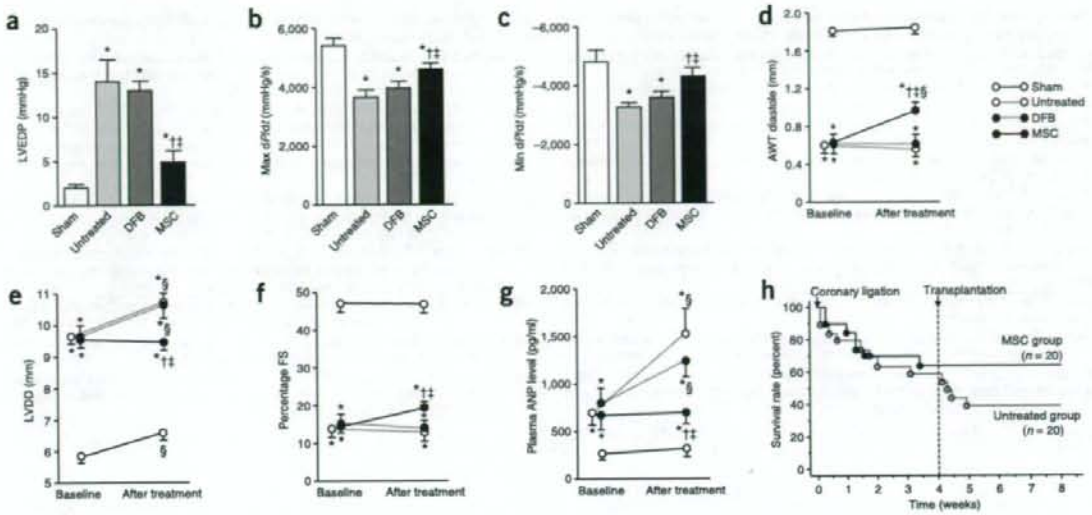

Figure 5 Cardiac structure and function after transplantation of monolayered MSCs. (**a–c**) Hemodynamic parameters obtained by catheterization. LVEDP, left ventricle end-diastolic pressure. (**d–f**) Echocardiographic findings. AWT, anterior wall thickness; LVDD, left ventricle end-diastolic dimension; FS, fractional shortening. (**g**) Plasma atrial natriuretic peptide (ANP) level. Baseline represents measurements 4 weeks after coronary ligation; 'after treatment' represents measurements taken 4 weeks after transplantation (8 weeks after coronary ligation). Data are mean ± s.e.m. $^{*}P < 0.05$ versus sham group; $^{\dagger}P < 0.05$ versus untreated group; $^{\ddagger}P < 0.05$ versus DFB group; $^{\S}P < 0.05$ versus baseline. (**h**) Survival of rats with chronic heart failure with or without monolayered MSC transplantation. The Kaplan-Meier survival curve demonstrates an 8-week survival rate of 65% for the MSC group versus 45% for the untreated group. Survival rate after transplantation was significantly higher in the MSC group than in the untreated group (100% versus 71% 4-week survival rate after transplantation, log-rank test, $P < 0.05$).

conditions at 37 °C and becomes reversibly hydrophilic below 32 °C. Therefore, cultured cells that adhere to the dish surface spontaneously detach from the grafted surface without enzymatic digestion.

Preparation of monolayered cell grafts. We suspended MSCs at the third or fourth passage from adipose tissue or DFBs at the second passage by trypsinization, and plated the cell suspension containing 3 ml of complete medium onto a 60-mm temperature-responsive dish at 5×10^5 cells per dish (MSCs) or 8×10^5 cells per dish (DFBs) and cultured cells at 37 °C. After 3 d of culture, confluently cultured MSCs or DFBs on the temperature-responsive dishes were incubated at 20 °C. By 40 min, both MSCs and DFBs detached spontaneously and floated up into the medium as monolayered cell grafts. Immediately after detachment, we gently aspirated the monolayered cell grafts using a 1,000 µl pipette tip and transferred them onto an elastic plastic sheet.

Statistical analysis. Numerical values are expressed as mean ± s.e.m. There are four groups of continuous variables in this study. Therefore, for multiple comparisons of more than two groups, we performed one-way analysis of variance (ANOVA). If the ANOVA was significant, we used the Newman-Keul procedure as a *post hoc* test. For repeated measurement such as echocardiographic parameters, we performed two-way repeated ANOVA with the Newman-Keul test. Comparisons of parameters between two groups were made by unpaired Student *t*-test. A value of $P < 0.05$ was considered significant.

Note: Supplementary information is available on the Nature Medicine website.

ACKNOWLEDGMENTS

We thank J.I. Hoffman for his statistical advice. We thank T. Iwase, T. Ito, S. Murakami, N. Sakata and Y. Isono for their technical support. We thank Y. Tsuboi and H. Sonoda for their assistance with microscopic analysis of monolayered cell grafts. We also thank Y. Sawa for his suggestions on this study. This work was supported by research grants for Cardiovascular Disease (16C-6) and Human Genome Tissue Engineering 005 and 009 from the Japanese Ministry of Health, Labor and Welfare, and the Program for Promotion of Fundamental Studies in Health Science of the Japanese National Institute of Biomedical Innovation.

COMPETING INTERESTS STATEMENT

The authors declare competing financial interests (see the *Nature Medicine* website for details).

Published online at http://www.nature.com/naturemedicine/
Reprints and permissions information is available online at http://npg.nature.com/reprintsandpermissions/

1. Liu, J. *et al.* Autologous stem cell transplantation for myocardial repair. *Am. J. Physiol. Heart Circ. Physiol.* **287**, H501–H511 (2004).
2. Reinlib, L. & Field, L. Cell transplantation as future therapy for cardiovascular disease?: A workshop of the National Heart, Lung, and Blood Institute. *Circulation* **101**, E182–E187 (2000).
3. Schuster, M.D. *et al.* Myocardial neovascularization by bone marrow angioblasts results in cardiomyocyte regeneration. *Am. J. Physiol. Heart Circ. Physiol.* **287**, H525–H532 (2004).
4. Kocher, A.A. *et al.* Neovascularization of ischemic myocardium by human bone-marrow-derived angioblasts prevents cardiomyocyte apoptosis, reduces remodeling and improves cardiac function. *Nat. Med.* **7**, 430–436 (2001).
5. Bel, A. *et al.* Transplantation of autologous fresh bone marrow into infarcted myocardium: a word of caution. *Circulation* **108**, II247–II252 (2003).
6. Yamada, N. *et al.* Thermo-responsive polymeric surface: control of attachment and detachment of cultured cells. *Makromol. Chem. Rapid Commun.* **11**, 571–576 (1990).
7. Okano, T., Yamada, H., Sakai, H. & Sakurai, Y. A novel recovery system for cultured cells using plasma-treated polystyrene dishes grafted with poly (N-isopropylacrylamide). *J. Biomed. Mater. Res.* **27**, 1243–1251 (1993).
8. Shimizu, T. *et al.* Fabrication of pulsatile cardiac tissue grafts using a novel 3-dimensional cell sheet manipulation technique and temperature-responsive cell culture surfaces. *Circ. Res.* **90**, e40–e48 (2002).
9. Hirose, M., Kwon, O.H., Yamato, M., Kikuchi, A. & Okano, T. Creation of designed shape cell sheets that are noninvasively harvested and moved onto another surface. *Biomacromolecules* **1**, 377–381 (2000).
10. Kushida, A. *et al.* Decrease in culture temperature releases monolayer endothelial cell sheets together with deposited fibronectin matrix from temperature-responsive culture surfaces. *J. Biomed. Mater. Res.* **45**, 355–362 (1999).
11. Herreros, J. *et al.* Autologous intramyocardial injection of cultured skeletal muscle-derived stem cells in patients with non-acute myocardial infarction. *Eur. Heart J.* **24**, 2012–2020 (2003).

12. Skobel, E. *et al.* Transplantation of fetal cardiomyocytes into infarcted rat hearts results in long-term functional improvement. *Tissue Eng.* **10**, 849–864 (2004).
13. Hodgson, D.M. *et al.* Stable benefit of embryonic stem cell therapy in myocardial infarction. *Am. J. Physiol. Heart Circ. Physiol.* **287**, H471–H479 (2004).
14. Makino, S. *et al.* Cardiomyocytes can be generated from marrow stromal cells in vitro. *J. Clin. Invest.* **103**, 697–705 (1999).
15. Pittenger, M.F. *et al.* Multilineage potential of adult human mesenchymal stem cells. *Science* **284**, 143–147 (1999).
16. Reyes, M. *et al.* Origin of endothelial progenitors in human postnatal bone marrow. *J. Clin. Invest.* **109**, 337–346 (2002).
17. Toma, C., Pittenger, M.F., Cahill, K.S., Byrne, B.J. & Kessler, P.D. Human mesenchymal stem cells differentiate to a cardiomyocyte phenotype in the adult murine heart. *Circulation* **105**, 93–98 (2002).
18. Wang, J.S. *et al.* Marrow stromal cells for cellular cardiomyoplasty: feasibility and potential clinical advantages. *J. Thorac. Cardiovasc. Surg.* **120**, 999–1005 (2000).
19. Jiang, Y. *et al.* Pluripotency of mesenchymal stem cells derived from adult marrow. *Nature* **418**, 41–49 (2002).
20. Nagaya, N. *et al.* Transplantation of mesenchymal stem cells improves cardiac function in a rat model of dilated cardiomyopathy. *Circulation* **112**, 1128–1135 (2005).
21. Rangappa, S., Fen, C., Lee, E.H., Bongso, A. & Wei, E.S. Transformation of adult mesenchymal stem cells isolated from the fatty tissue into cardiomyocytes. *Ann. Thorac. Surg.* **75**, 775–779 (2003).
22. Zuk, P.A. *et al.* Human adipose tissue is a source of multipotent stem cells. *Mol. Biol. Cell* **13**, 4279–4295 (2002).
23. Gaustad, K.G., Boquest, A.C., Anderson, B.E., Gerdes, A.M. & Collas, P. Differentiation of human adipose tissue stem cells using extracts of rat cardiomyocytes. *Biochem. Biophys. Res. Commun.* **314**, 420–427 (2004).
24. Planat-Benard, V. *et al.* Plasticity of human adipose lineage cells toward endothelial cells: physiological and therapeutic perspectives. *Circulation* **109**, 656–663 (2004).
25. Lee, R.H. *et al.* Characterization and expression analysis of mesenchymal stem cells from human bone marrow and adipose tissue. *Cell. Physiol. Biochem.* **14**, 311–324 (2004).
26. Li, J., Takaishi, K., Cook, W., McCorkle, S.K. & Unger, R.H. Insig-1 "brakes" lipogenesis in adipocytes and inhibits differentiation of preadipocytes. *Proc. Natl. Acad. Sci. USA* **100**, 9476–9481 (2003).
27. Vande Berg, J.S., Rudolph, R. & Woodward, M. Comparative growth dynamics and morphology between cultured myofibroblasts from granulating wounds and dermal fibroblasts. *Am. J. Pathol.* **114**, 187–200 (1984).
28. Nishida, K. *et al.* Corneal reconstruction with tissue-engineered cell sheets composed of autologous oral mucosal epithelium. *N. Engl. J. Med.* **351**, 1187–1196 (2004).
29. Shimizu, T., Yamato, M., Kikuchi, A. & Okano, T. Cell sheet engineering for myocardial tissue reconstruction. *Biomaterials* **24**, 2309–2316 (2003).
30. Nishikimi, T., Uchino, K. & Frohlich, E.D. Effects of α1-adrenergic blockade on intrarenal hemodynamics in heart failure rats. *Am. J. Physiol. Regul. Integr. Comp. Physiol.* **262**, R198–R203 (1998).

The EMBO Journal (2006) 25, 2315–2325 | © 2006 European Molecular Biology Organization | All Rights Reserved 0261-4189/06
www.embojournal.org

THE EMBO JOURNAL

Crystal structure of CHP2 complexed with NHE1-cytosolic region and an implication for pH regulation

Youssef Ben Ammar[1,4], Soichi Takeda[2,3,4], Takashi Hisamitsu[1], Hidezo Mori[2] and Shigeo Wakabayashi[1,*]

[1]Department of Molecular Physiology, National Cardiovascular Center Research Institute, Suita, Osaka, Japan, [2]Department of Cardiac Physiology, National Cardiovascular Center Research Institute, Suita, Osaka, Japan and [3]Laboratory of Structural Biochemistry, RIKEN Harima Institute at SPring-8, Kouto, Mikazuki-cho, Sayo, Hyogo, Japan

The plasma membrane Na^+/H^+ exchangers (NHE) require calcineurin B homologous protein (CHP) as an obligatory binding partner for ion transport. Here, we report the first crystal structure of CHP (CHP2 isoform) in complex with its binding domain in NHE1. We show that the cytoplasmic α-helix of NHE1 is inserted into the hydrophobic cleft formed by N- and C-lobes of CHP2 and that the size and shape of this crevice together with hydrogen bond formation at multiple positions assure a high degree of specificity for interaction with NHE members. Structure-based mutagenesis revealed the importance of hydrophobic interactions between CHP/NHE1 for the function of NHE1. Furthermore, the crystal structure shows the existence of a protruding CHP-unique region, and deletion of this region in CHP2 inhibited the NHE1 activity by inducing the acidic shift of intracellular pH dependence, while preserving interaction with NHE1. These findings suggest that CHP serves as an obligatory subunit that is required both for supporting the basic activity and regulating the pH-sensing of NHE1 via interactions between distinct parts of these proteins.

The EMBO Journal (2006) **25**, 2315–2325. doi:10.1038/sj.emboj.7601145; Published online 18 May 2006
Subject Categories: membranes & transport; structural biology
Keywords: calcineurin homologous protein; crystal structure; Na^+/H^+ exchanger; pH regulation

Introduction

Maintenance of intracellular pH (pH_i), Na^+ concentration, and cell volume is crucial for all living cells to survive and to ensure a variety of cellular functions, such as cell metabolic processes, muscle contraction, secretion, and higher-order brain activity. The Na^+/H^+ exchanger (NHE) is an important transporter regulating such ionic homeostasis and catalyzing the electroneutral countertransport of Na^+ and H^+ through the plasma membrane and other intracellular organellar membranes in various animal species (Wakabayashi *et al*, 1997; Counillon and Pouyssegur, 2000; Putney *et al*, 2002; Orlowski and Grinstein, 2004; Zachos *et al*, 2005). Of the nine different NHE isoforms identified to date (NHE1–NHE9), the ubiquitous isoform NHE1 has been studied most extensively. NHE1 is known to be activated rapidly in response to various extracellular stimuli, such as hormones, growth factors, and mechanical stressors (Wakabayashi *et al*, 1997; Orlowski and Grinstein, 2004). Such activation of NHE1 is often linked to various diseases. For example, elevated NHE1 activity is thought to be a risk factor causing heart failure and hypertrophy, as evidenced by the remarkable protective effects of specific inhibitors (Karmazyn, 2001; Engelhardt *et al*, 2002). Regulation of NHE1 is thought to occur through interaction of multiple signaling molecules with the carboxyl (C)-terminal cytoplasmic domain of NHE1 and subsequent conformational change of the amino (N)-terminal transmembrane domain responsible for catalyzing NHE (see Figure 1A for membrane topology). Importantly, this regulation of NHE1 is attributable to a change in the affinity for intracellular H^+. A previous biochemical experiment using membrane vesicles suggested that the exchangers possess a cytoplasmic 'H^+-modifier' or 'pH-sensor' site(s), distinct from the H^+-transport site (Aronson *et al*, 1982; Wakabayashi *et al*, 2003a). The exchangers were thus considered to be activated through conformational changes caused by protonation of this regulatory site. Our recent study, using cells expressing NHE isoforms (NHE1–3), further supported this concept by measuring the reverse reaction of exchange (Na^+ efflux) (Wakabayashi *et al*, 2003a). However, another recent study reported an allosteric model with no additional H^+-modifier site to explain the sigmoidal cytosolic H^+ dependence (Lacroix *et al*, 2004).

Of the signaling molecules that interact with the exchanger, calcineurin B (CNB) homologous protein (CHP) is particularly important. CHP was initially identified as a protein (p22) involved in vesicular transport (Barroso *et al*, 1996) and that interacts with NHE (Lin and Barber, 1996). CHP is a Ca^{2+}-binding protein with EF-hand motifs and is myristoylated at the N-terminus (Gly2) (Barroso *et al*, 1996; Lin and Barber, 1996). To date, three CHP isoforms with different tissue expression patterns have been identified in mammalian tissues. While CHP1 is expressed ubiquitously in virtually all tissues, the expression of CHP2 is restricted to cancer cells (Pang *et al*, 2002) and the small intestine (Inoue *et al*, 2003), and that of CHP3 (also called tescalcin) is restricted to the heart, brain, stomach, and testis (Mailander *et al*, 2001; Perera *et al*, 2001; Gutierrez-Ford *et al*, 2003). Previously, we reported that CHP (at least CHP1 and CHP2) is an essential cofactor supporting the physiological activity of the plasmalemmal NHE by interacting with the juxtamembrane cyto-

*Corresponding author. Department of Molecular Physiology, National Cardiovascular Center Research Institute, Fujishirodai 5-7-1, Suita, Osaka 565-8565, Japan. Tel.: +81 6 6833 5012; Fax: +81 6 6835 5314; E-mail: wak@ri.ncvc.go.jp
[4]These authors contributed equally to this work

Received: 5 December 2005; accepted: 24 April 2006; published online: 18 May 2006

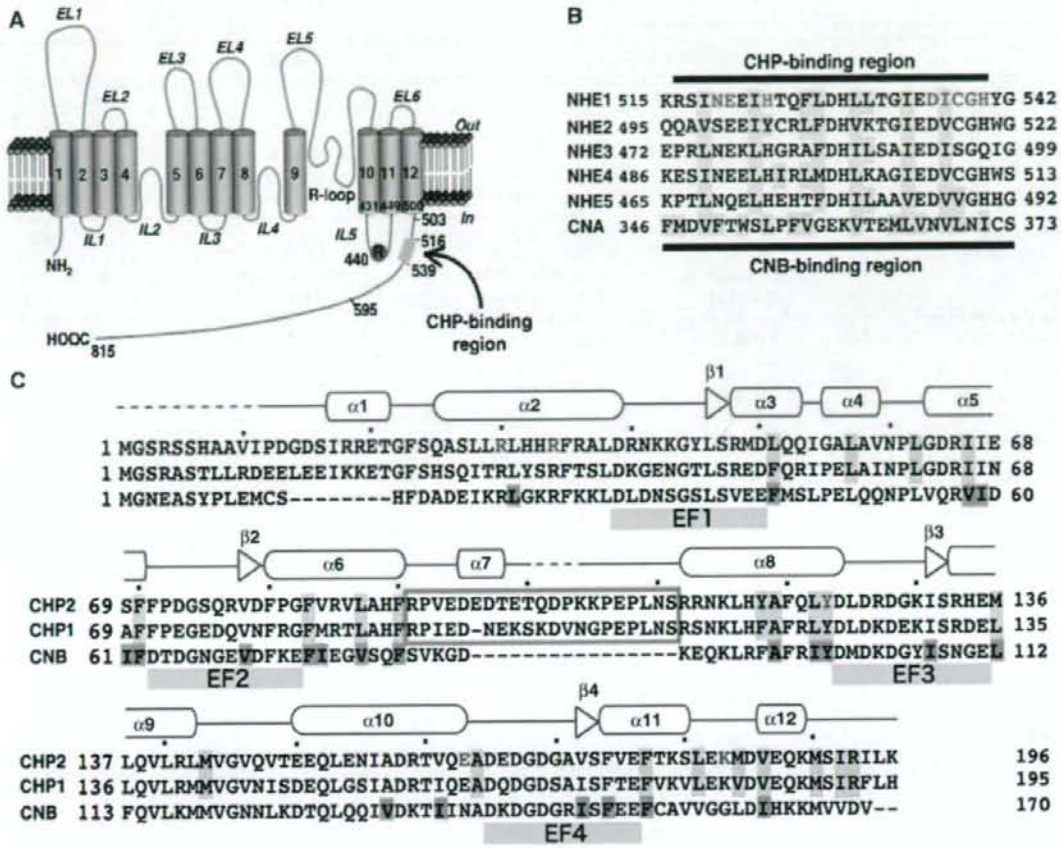

Figure 1 Sequence alignments of CHP and its binding domain in NHE isoforms. (**A**) Membrane topology model of NHE1. NHE1 consists of the N-terminal transporter domain with 12 transmembrane domains (TM) and a long C-terminal regulatory domain. Six extracellular (EL) and five intracellular loops (IL) are mapped. CHP binds to the juxtamembrane cytoplasmic domain. Arg440 was identified as an important residue for NHE1 regulation. (**B**) Amino-acid sequences for human NHE1–NHE5 (Genbank Accession Numbers: NM_003047, NM_003048, NM_004174, NM_177084, and NM_004594, respectively) are aligned together with sequence of CNB-binding region in CNA (Q08209). Hydrophobic residues involved in interaction with CHP or CNB are highlighted in green. Residues in NHE1 forming hydrogen bonds with CHP2 are shown in *red*. (**C**) Amino-acid sequences of CHP1/2 and CNB (Q99653, Q9D869, and P63098). Secondary structural elements are based on the structure of CHP2/NHE1-peptide complex. Loops of four EF-hands are shown by *green* boxes, but EF1 and EF2 are ancestral sites that do not coordinate Ca^{2+}. Hydrophobic residues involved in interaction with NHE1 or CNA are highlighted in *blue* and *red*, respectively. Central CHP-unique region is *boxed*. Residues in CHP2 forming hydrogen bonds with NHE1 are shown in *red*.

plasmic domain of NHE1 to NHE3 (Pang *et al*, 2001, 2002). CHP binding-defective mutant exchangers (NHE1-3) exhibited low exchange activity (Pang *et al*, 2001) (5–10% of the wild-type level) and greatly shifted the pH_i-dependence to the acidic side (Pang *et al*, 2004), suggesting that the juxtamembrane region with bound CHP would therefore function as a key structure maintaining the physiologically active conformation of NHE1. Recently, the crystal structure of CHP1 was solved as a single polypeptide without the target molecule (Naoe *et al*, 2005). However, this structure did not provide information about the interaction(s) with NHE.

To obtain insights into the molecular mechanisms of the interaction(s) with NHE and regulation of NHE by CHP, we determined the crystal structure of CHP (CHP2 isoform) complexed with its binding region in NHE1. Herein, we report that the α-helical CHP-binding region of NHE1 is inserted into the hydrophobic cleft formed by residues in the N- and C-lobes of CHP2 through strong hydrophobic interactions as well as hydrogen bond formation. Structure-based mutational analysis revealed that CHP may activate the exchanger by associating its hydrophobic cleft and also regulate the pH-sensing of NHE1 via its central CHP-unique region connecting the two lobes of CHP.

Results

Overall structure of CHP2 in complex with the cytoplasmic binding region of NHE1

We crystallized the His_6-tagged human CHP2 (1–196) complexed with its binding domain (aa 503–545) in NHE1 (referred to as CHP2/NHE1-peptide) in the presence of yttrium, initially solved the structure by MAD phasing, and refined the structure model to 2.7 Å (Table I). Figure 2 shows

Table I Data collection, phasing and refinement statistics

	High resolution data	MAD		
Data collection				
Space group	$P4_3$		$P4_3$	
Cell dimensions				
a, *b*, *c* (Å)	49.96, 49.96, 103.2		49.96, 49.96, 103.2	
α, β, γ (deg)	90, 90, 90		90, 90, 90	
		Peak	*Inflection*	*Remote*
Wavelength	1.0000	0.7270	0.7266	1.0000
Resolution (Å)	50–2.7	50–3.0 (3.11–3.00)	50–3.0 (3.11–3.00)	50–3.0 (3.11–3.00)
R_{merge}[a]	4.8 (25.1)	0.084 (0.311)	0.073 (0.297)	0.072 (0.330)
$I/\sigma I$[b]	17.3 (4.5)	14.9 (4.1)	15.9 (5.0)	15.8 (3.6)
Completeness (%)[b]	97.3 (83.1)	98.5 (87.5)	98.5(87.5)	97.8 (80.9)
Redundancy[b]	4.0 (3.1)	7.2 (5.6)	7.3 (5.7)	7.1 (5.3)
Refinement				
Resolution (Å)	50–2.7			
No. reflections	6746			
R_{work}/R_{free}	0.218/0.287			
No. atoms				
Protein	1674			
Ligand/ion	2			
B-factors				
Protein	72.5			
Ligand/ion	70.5			
R.m.s. deviations				
Bond lengths (Å)	0.005			
Bond angles (deg)	1.00			
Ramachandran plot (%)				
Favorable	87.2			
Allowed	12.8			
Generously allowed	0			
Disallowed	0			

[a]$R_{merge} = \sum_{hkl} \sum_i |I_i(hkl) - \langle I(hkl) \rangle| / \sum_{hkl} \sum_i I_i(hkl)$, where $I_i(hkl)$ is the *i*th intensity measurement of reflection *hkl*, and $\langle I(hkl) \rangle$ is its average.
[b]Highest resolution shell is shown in parentheses.

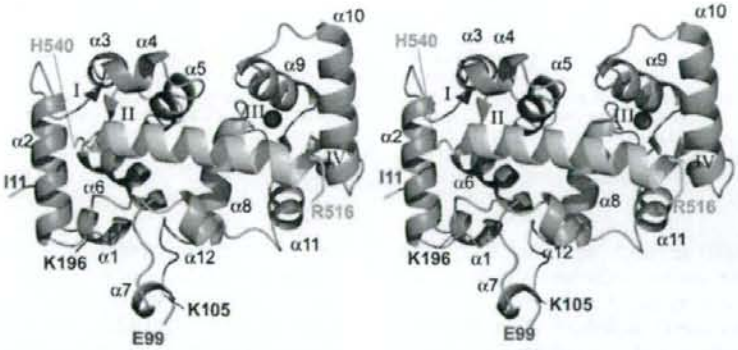

Figure 2 Stereo view of the CHP2/NHE1-peptide complex showing the overall structure. N- and C-lobes of CHP2 are colored *red* and *blue*, respectively. The NHE1 peptide is colored *green*. *Pink* spheres represent the two yttrium ions coordinated by EF3 and EF4.

the overall structure of the complex CHP2/NHE1-peptide. The structural model contains 181 amino acids from CHP2 (Ile11–Glu99 and Lys105–Lys196), and 25 amino acids from NHE1 fragment (Arg516–His540). The polypeptide chain of CHP2 with dimensions of $55 \times 47 \times 28$ Å is folded into two globular domains (N- and C-terminal lobes) composed of 12 α-helices (α1–α12) and four short β-strands (β1–β4). Two Y^{3+} ions were found to associate with EF3 and EF4 in the C-lobe (Figure 2), consistent with biochemical data showing the high-affinity binding of Y^{3+} (~1 nM) to CHP2 (Supplementary Figure 1). The overall structure of CHP2 is close to the Ca^{2+}-bound form of NHE-free CHP1, which was solved recently (Naoe *et al*, 2005; Supplementary Figure 2). Indeed, the distances between metal ions and coordinating oxygen atoms are almost the same for Y^{3+} in CHP2 (2.38 ± 0.2 Å) and Ca^{2+} in CHP1 (2.40 ± 0.1 Å). In addition, the

Y^{3+}-bound form of CHP2 preserved the ability to interact with the full-length NHE1 (Supplementary Figure 1). Therefore, we consider our solved structure compatible with the Ca^{2+}-bound form of CHP2. The overall structure of CHP2 is also similar in folding topology to the structures of other EF-hand-containing proteins, including CNB (Kissinger *et al*, 1995), K^+-channel interacting protein (KChIP1) (Zhou *et al*, 2004; Supplementary Figure 2), AtCBL2 (Nagae *et al*, 2003), NCS-1 (Bourne *et al*, 2001), neurocalcin (Vijay-Kumar and Kumar, 1999), and CIB (Gentry *et al*, 2005). A common structural feature of these proteins is that they all have four EF-hands in pairs such that EF1 and EF2 form the N-lobe and EF3 and EF4 form the C-lobe. However, some local differences were observed between CHP2 and CNB or between CHP2 and KChIP1. For example, the orientation of EF-hand α-helices is different among these molecules because of the swiveling motion between the N- and C-lobes of each molecule, although each pair of EF hands is relatively fixed via hydrogen bonds. This may explain the incomplete superposition between overall structures of CHP2 and CNB (root mean square deviation, r.m.s.d. 1.7 Å), in contrast to the relatively good superposition between the N-lobes or between the C-lobes themselves (r.m.s.d. 1.3 or 1.0 Å, respectively). Although CHP2 and CNB have about 36% identity in their amino-acid sequences (Figure 1C), CHP2 coordinates two Ca^{2+} ions in EF3 and EF4, unlike CNB capable of coordinating four Ca^{2+} ions in its four EF-hands (Kissinger *et al*, 1995). Lack of Ca^{2+}-coordination in EF1 and EF2 would be derived from significant deviation from the canonical EF-hand sequence and resulting atypical structure, as described previously in detail (Naoe *et al*, 2005).

The most remarkable difference between CHP2 and other calcium binding proteins is that the N- and C-lobes of CHP2 are linked by a long flexible region, which protrudes by a length of about 14 Å for the determined region (Figure 3A). This domain, referred to as the CHP-unique region, was not found in other Ca^{2+}-binding proteins. Five residues, Thr100 to Lys104, were not assigned in the structure due to the absence of their electron density map. Particularly, the region from aa 93–108 did not make any contact with other regions of CHP2. In addition, we found that the side chain oxygen atoms of Asp95 in this region coordinate Y^{3+} in the neighboring molecule in the crystal and thus participate in stabilization of this region. This observation explains why CHP2/NHE1-peptide was crystallized only in the presence of Y^{3+}. These findings suggest that the CHP-unique region is very flexible in aqueous solution. This is consistent with the finding that this region was not seen in the structure of NHE-free CHP1 (Naoe *et al*, 2005), which was solved in different crystal packing.

Interaction between CHP2 and its binding domain in NHE1

Structure determination of the complex revealed the orientation of CHP2 toward the cytoplasmic region of NHE1. The N- and C-terminal halves of the cytoplasmic α-helix of NHE1 are inserted into the hydrophobic cleft in such a way that they face the C- and N-lobes of CHP2, respectively (Figure 3A). This cleft constitutes the region that traps the cytoplasmic α-helix of NHE1 and maintains the stability of the complex by means of hydrophobic interactions. The contact area between CHP2- and NHE1 peptide is 1466 $Å^2$, which accounts for 13.0

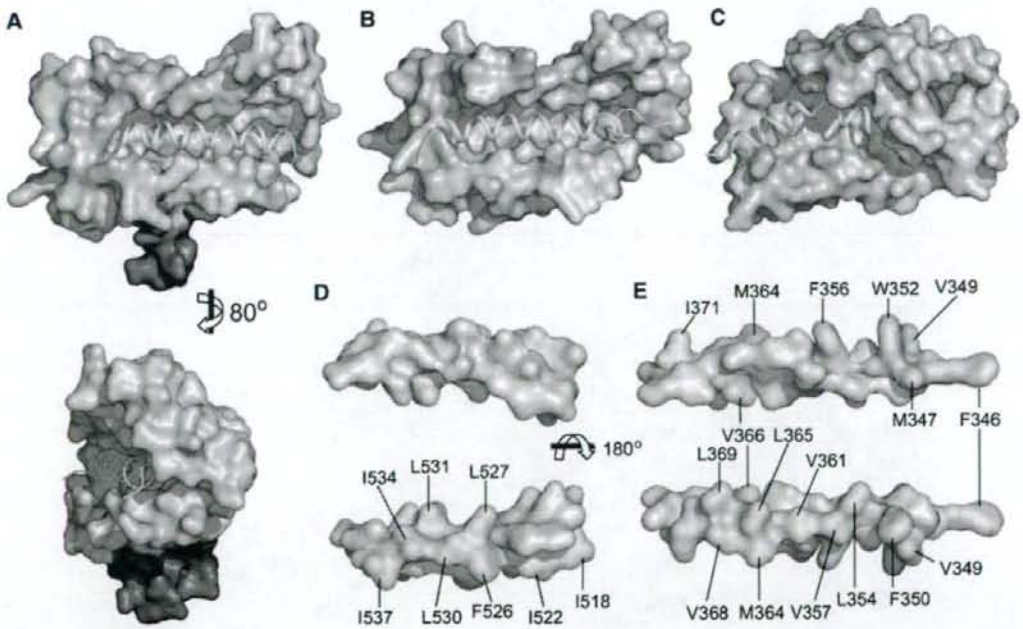

Figure 3 Target specificity of hydrophobic cleft. **(A–C)** Surface features of CHP2, CNB, and KChP1 are presented together with α-helices of target peptides, respectively. In CHP2, front (*upper*) and side (*lower*) views are shown. The N- and C-lobes are colored *light blue* and *light green*, while the CHP-unique region is colored *red*. **(D, E)** Surface view of NHE1 (*left*) and CNA (*right*) peptides, respectively. The *upper* panels indicate the side facing outside the cleft and the *lower* panels represent the side facing the cleft. Hydrophobic residues are colored *yellow*.

and 59.8% of the total surface areas, respectively, implying that a large area is used for interaction between the two molecules. The NHE1 peptide (Arg516–His540) solved in this structure contains different hydrophobic residues, all of which face toward the hydrophobic cleft of CHP2 (Figure 3D). Ile518, Ile522, Phe526, Leu527, and Leu530 are accommodated into the cavity formed by hydrophobic residues provided mainly from the C-lobe of CHP2, whereas Leu531, Ile534, and Ile537 are inserted into the cavity formed mainly by the N-lobe of CHP2 (Figure 4A and B). All hydrophobic side chains of the NHE1 peptide, with the exception of Ile518, make van der Waals contacts with side chain atoms from many hydrophobic residues of CHP2. For example, side chain atoms of Ile534 make van der Waals contacts with those of Leu57, Ile66, Phe70, Val86, Leu87 Phe90, Tyr118, and Ile192 of CHP2 (Figure 4C), while side chain atoms of Leu527 make interactions with those of Ala119, Leu181, Val186, Met184, and Met190 (Figure 4A). In addition to hydrophobic interactions, hydrogen bonds strengthen the association between CHP2 and NHE1 peptide. In the N-lobe of CHP2, the guanidinium group of Arg30 makes hydrogen bonds with the main chain carbonyl oxygen of Gly539, while the guanidinium group of Arg34 makes hydrogen bonds with the main chain carbonyl oxygens of Asp536 and Ile537 (Figure 4B). These hydrogen bonds are very important for the C-terminal end of the NHE1 helix to fix to the edge of the hydrophobic cleft of CHP2. The conserved Gly539 residue of NHE1 would allow the following cytoplasmic stretch to leave the cleft by inducing clear bending of the NHE1 peptide (Figures 3A and 4B). Several other hydrogen bonds are also formed. The hydrogen bond between the imidazole group (Nδ) of His523 in NHE1 and the side chain oxygen of Tyr123 in CHP2 is particularly interesting because it is the only polar interaction in the hydrophobic surface of the cleft (Supplementary Figure 3). These polar interactions are important to determine the specificity and orientation of CHP2 toward the cytoplasmic α-helix of NHE1.

Although CNB and KChIP1 have similar hydrophobic clefts (Figure 3B and C), their size and shape are clearly different from those of CHP2. Interestingly, target peptides show sequence features that just fit to their clefts. While NHE1 peptide shows a uniform distribution of hydrophobic residues all facing toward the cleft of CHP2 (Figure 3D), CNA contains more hydrophobic residues that face toward both the CNB crevice and the outside (Figure 3E). In addition, CNA peptide contains four aromatic residues (Phe346, Phe350, Trp352, and Phe356) in the N-terminus, which are accommodated in corresponding hydrophobic cavities in the C-lobe of CNB, whereas NHE1-peptide contains only one aromatic residue (Phe526) located in the central part of CHP2. These observations suggest that highly selective fitting of each peptide to its corresponding crevices may be caused by differences in the distribution of hydrophobic residues of the target peptides and in the shape of the cleft formed by α-helices of EF-hands.

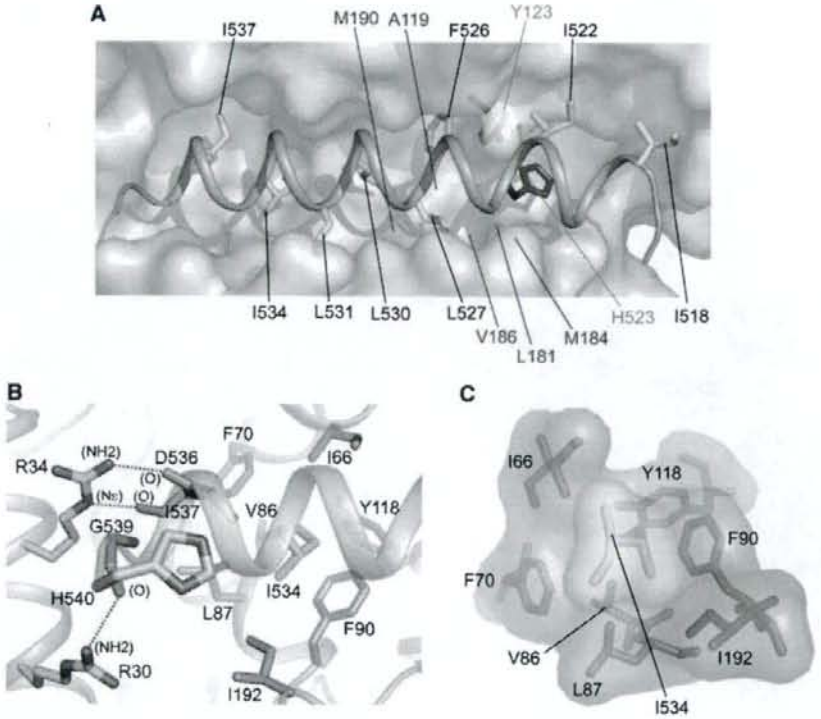

Figure 4 Closeup view showing the interaction between CHP2 and NHE1-peptide. (**A**) The NHE1-peptide backbone is shown in *magenta*, while hydrophobic side chains are shown in *yellow*. The hydrophobic pocket surrounding Leu527 is marked in *red*. His523 of NHE1 and Tyr123 of CHP2 are marked in *blue*. (**B**) Closeup view showing interaction between the N-lobe of CHP2 and the C-terminus of NHE1-peptide. (**C**) Ile534 is accommodated into the hydrophobic pocket produced by residues mainly in the N-lobe of CHP2.

Effect of mutations on interaction between NHE1 and CHP2 in cells

The present structure indicated that the correct CHP-binding domain of NHE1 consists of the region from aa 516–540, extended by 10 residues toward the C-terminus of the region (aa 510–530), as predicted previously (Pang *et al*, 2001). This prompted us to mutate residues in this extended region of NHE1 interacting with the N-lobe of CHP2. We mutated the Ile534 and Ile537 residues of NHE1 into charged residues (Lys or Asp) and stably expressed these mutants in exchanger-deficient PS120 cells. These mutants were expressed in the plasma membrane (as indicated by the existence of surface-expressed mature NHE1 in Supplementary Figure 4). We examined the interactions of these mutants with CHP2 by assessing whether stably transfected green fluorescent protein (GFP)-tagged CHP2 was localized to the plasma membrane. As shown in Figure 5A, most of the CHP2 was localized to the plasma membrane of cells expressing the wild-type NHE1 but not in nontransfected PS120 cells (not shown; see Pang *et al*, 2001), indicating a strong interaction. Of note, in most cells expressing the wild-type NHE1 almost no GFP-fluorescence was detected in the intracellular space (Figure 5A), despite the accumulation of immature NHE1 in the intracellular membranes under forced expression (data not shown), suggesting that CHP2 interacts predominantly with mature NHE1 in the plasma membrane. This was further confirmed by the finding that almost no immature NHE1 co-immunoprecipitated with CHP2 (Supplementary Figures 1 and 4). In contrast to the wild-type NHE1, the plasma membrane localization of CHP2 was almost completely abolished when transfected into cells expressing the NHE1 mutants, I534K, I534D and I537K (Figure 5, and also D for summarized data), indicating that these mutations drastically reduced the affinity for interaction with CHP2.

Furthermore, as expected, the plasma membrane localization of CHP2 was also markedly reduced in cells expressing the wild-type NHE1 when Leu87 or Tyr118 of CHP2 was changed to Lys (Figure 5C and D), indicating that these mutants are not able to replace completely endogenous CHP1 bound to NHE1. As the expression of GFP-tagged CHP2 was approximately 10-fold higher than that of endogenous CHP1 (data not shown), these results suggest that these mutations would reduce the affinity for interaction with NHE1 at least one-order of magnitude. Similar analysis was performed with mutation of the Arg residues (Arg30 and Arg34) in the N-terminal α-helix of CHP2. The plasma membrane localization of CHP2 was abolished when these two residues were simultaneously changed to Glu (Figure 5C and D), while it was still partially preserved when either Arg residue alone was changed to Glu. Similar results were also obtained for the NHE1/CHP2 interaction in a co-immunoprecipitation experiment (Supplementary Figure 4). Thus, the hydrophobic and polar interactions involving these residues would be important in determining the strong and highly specific association between NHE1 and CHP2, Furthermore, in addition to the C-lobe, the N-lobe of CHP2 plays a crucial role in the tight interaction with NHE1, suggesting that our crystal structure reflects the interaction between native NHE1 and CHP2 molecules expressed in cells. On the other hand, structure determination indicated the existence of a unique protruding region in CHP2. In contrast to mutations of residues involving formation of the cleft, a mutant with deletion of this CHP-unique region (Δ94–104) was mostly localized to the plasma membrane of cells expressing wild-type NHE1 (Figure 5C), indicating that deletion did not disrupt the interaction of CHP2/NHE1. Hence, as also predicted from structure, the CHP-unique region was not involved in the interaction between CHP2/NHE1. The 10 N-terminal residues of CHP2 were also found not to be involved in the interaction, as indicated by the plasma membrane localization of ΔN10 (Figure 5C).

Functional consequence of mutations

We measured the NHE activity in cells expressing mutant exchangers. Figure 6A demonstrates the pH_i-dependence of EIPA-sensitive $^{22}Na^+$-uptake activity. While the wild-type NHE1 exhibited high $^{22}Na^+$-uptake activity, with pK ~6.5 for pH_i (Hill coefficient, ~1.7), the activity of mutant exchangers, I534D, I534K and Ile537, which lack CHP-binding was very low (see Supplementary Table I for kinetic parameters). The inhibitory effect of the mutations was characterized by changes in two parameters: (i) a drastic reduction of maximal $^{22}Na^+$-uptake activity (V_{max}) at acidic pH_i, and (ii) a large acidic shift of the pH_i-dependence of uptake (>0.6 pH units) (see Figure 6A, inset for normalized activity). We then compared the pH_i-dependence of $^{22}Na^+$-uptake in cells co-expressing NHE1 with GFP-tagged CHP2 or its deletion mutant Δ94–104, which preserves interaction with CHP. Interestingly, expression of Δ94–104 significantly shifted the pH_i-dependence of uptake towards acidic pH_i (~0.2 pH unit) without any change in V_{max}, while it preserved the cooperative pH_i dependence, with a Hill coefficient ~1.5 (Figure 6B, see also inset for the sigmoidal internal H^+ dependence), suggesting that the CHP-unique region is involved in regulation of pH-sensing of NHE1. In general, the sigmoidal H^+-dependence has been interpreted as exhibiting involvement of at least two H^+-binding sites: H^+-transport and H^+-regulatory sites in NHE (Wakabayashi *et al*, 1997). To examine the effect of deletion of a CHP-specific region on the H^+-regulatory site, we measured the reverse reaction of NHE1, that is, $^{22}Na^+$ efflux coupled to H^+-influx. If we assume that NHE1 catalyzes a counter-transport reaction only involving the transport site, intracellular acidification should result in inhibition of $^{22}Na^+$ efflux due to cytosolic Na^+/H^+ competition. In contrast to this thermodynamically expected inhibition, modest acidification from 7.5 to 7.2 dramatically stimulated the rate of EIPA-inhibitable $^{22}Na^+$ efflux in cells co-expressing the wild-type NHE1 and CHP2 (Figure 6D), suggesting that protonation of H^+-regulatory sites activated NHE1 (Figure 6C), as reported in detail, previously (Aronson *et al*, 1982; Wakabayashi *et al*, 2003a). Consistent with the acidic shift of pH_i-dependence of $^{22}Na^+$ uptake, we observed that deletion of a CHP-unique region significantly reduced the rate of $^{22}Na^+$ efflux (Figure 6D). EIPA-sensitive fraction of $^{22}Na^+$ efflux at pH_i 7.2 during the initial 3 min was reduced to ~30% upon expression of Δ94–104, suggesting that the affinity of the H^+-regulatory site for H^+ decreased upon deletion of this region.

Discussion

In the present study, we solved the first crystal structure of the CHP2/NHE1-peptide complex at 2.7 Å. This structure provides detailed information regarding the interaction between

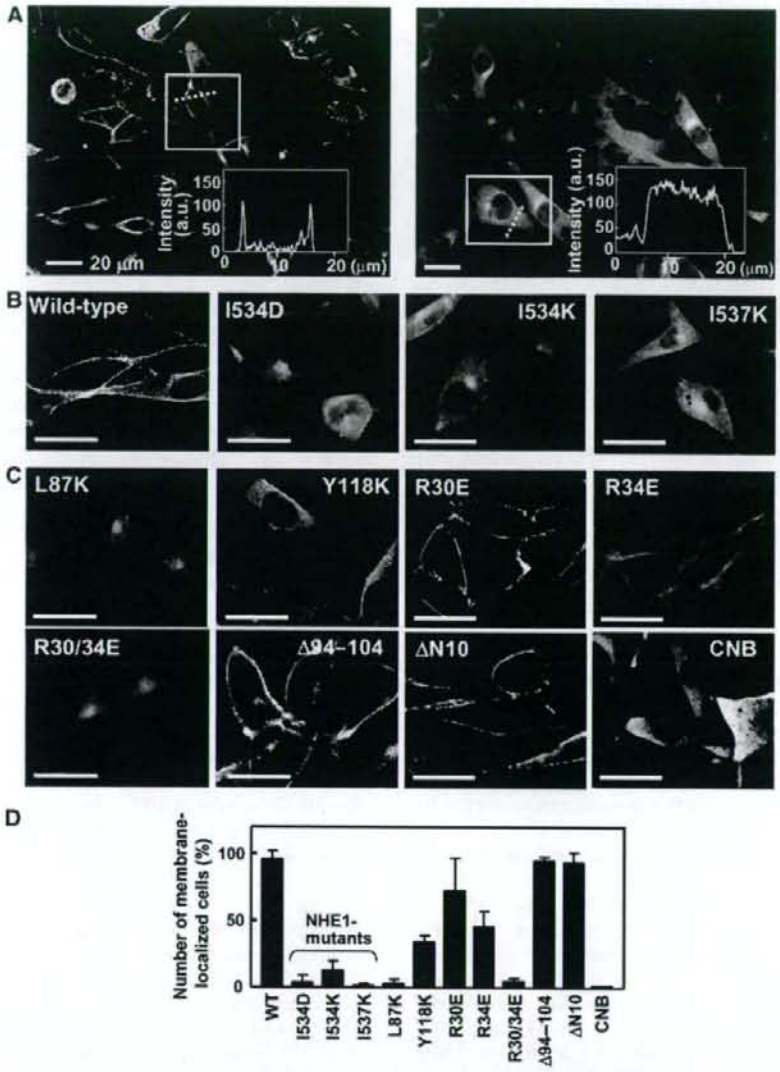

Figure 5 Effects of mutations on the interaction between NHE1 and CHP2 in cells. (**A**) Low magnification confocal images of cells coexpressing GFP-tagged CHP2 and the wild-type (*left*) or I537K (*right*) mutant exchangers. Inset shows the intensity profile of GFP fluorescence along the dotted line in a marked cell. In most cells expressing the wild-type NHE1 but not I537K, strong fluorescent signals were detected at the cell edge. (**B**) Subcellular localization of CHP2 expressed in cells. GFP-tagged CHP2 was coexpressed in cells stably expressing the wild-type or mutant NHE1 variants and GFP-fluorescence was observed by confocal microscopy. (**C**) Subcellular localization of mutant CHP2. GFP-tagged CHP2 mutants were expressed in cells stably expressing the wild-type NHE1. Eleven residues from Glu94 to Lys104 of CHP2 were deleted in Δ94–104, while the 10 N-terminal residues from Met1 to Val10 were deleted in ΔN10. For one control experiment, GFP-tagged human CNB was expressed in NHE1-transfectants. (**D**) Summary data for membrane localization of GFP-tagged CHP2. Intensity profile analysis was performed on confocal images as shown in (A). The number of cells with strong fluorescence signal at the cell edge (at least three times more than the average of fluorescence in the internal cell region) was counted. Data are expressed as the mean ± s.d. from 6–8 images (total cell number analyzed, 99–341).

NHE1 and CHP: (i) the interaction with NHE1 occurs in a hydrophobic cleft encompassing the N- and C-lobes of CHP2, (ii) this interaction occurs by extensive Van der Waals contact between hydrophobic residues, as well as by some specific hydrogen bonds, (iii) the interacting region of NHE1 forms an α-helix which bends at a conserved Gly539 and (iv) two domains of CHP2 are connected by a large flexible CHP-unique region. These features strengthened our previous functional study (Pang *et al*, 2001, 2002, 2004) from structural aspects and at the same time provided new information to be addressed regarding the function of NHE1.

A unique feature of interaction between CHP and NHE

Structure comparison among Ca^{2+}-binding proteins provided valuable information regarding the target specificity of CHP1/2 proteins. Although the crystal structure of CNB/CNA com-

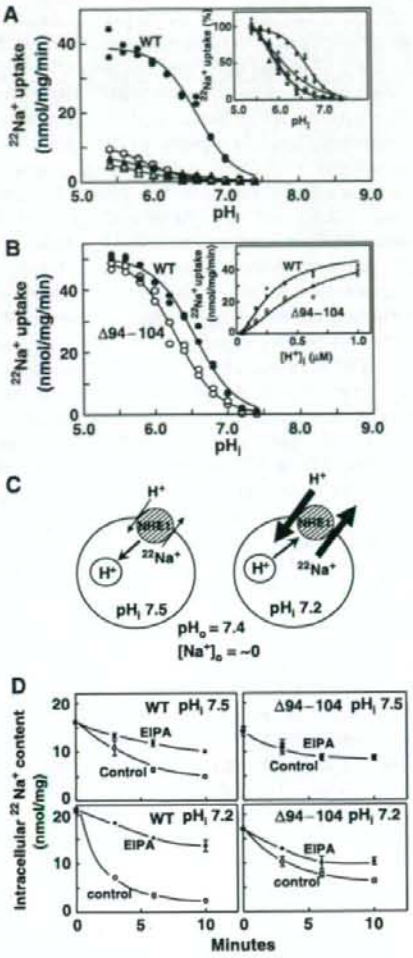

Figure 6 Effect of mutations on the exchange activity. (**A**), pH_i-dependence of EIPA-sensitive $^{22}Na^+$-uptake in cells expressing wild-type NHE1 (●) or CHP binding-defective mutants, I534D (○), I534K (▲) and I537K (△). pH_i was clamped at various values with K^+/nigericin. Data were fitted to Hill equations with the kinetic parameters shown in Supplementary Table I and plotted after normalization by the maximal activity at $pH_i = 5.4$ (*inset*). (**B**) pH_i-dependence of EIPA-sensitive $^{22}Na^+$-uptake in cells co-expressing wild-type NHE1 and GFP-tagged CHP2 (●) or deletion mutant Δ94–104 of CHP2 (○). Data were fitted to Hill equations with the kinetic parameters shown in Supplementary Table I. The $^{22}Na^+$-uptake activity was also plotted against intracellular H^+ concentration up to 1 μM (*inset*). (**C**) Schematic drawing of $^{22}Na^+$-efflux protocol. The efflux experiment was done in $^{22}Na^+$-loaded, pH_i-clamped cells at extracellular pH 7.4. At lower pH_i $^{22}Na^+$ efflux would be accelerated by H^+ binding to the regulatory site, while at high pH_i it would be inhibited by H^+-release from the regulatory site. (**D**) Time courses of $^{22}Na^+$ efflux. Cells were loaded with $^{22}Na^+$ and at the same time pH_i-clamped at pH_i 7.5 or 7.2. After removal of the radioactive solution, cells were exposed to the nonradioactive solutions with or without 0.1 mM EIPA. Data are expressed as the mean ± s.d. of three determinations. Error bars are sometimes smaller than symbol sizes.

plex (Kissinger *et al*, 1995) revealed a similar mode of interaction through its hydrophobic groove, comparison between the hydrophobic clefts of CHP2 and CNB showed several different structural features (Figure 3A and B). In addition, there is a marked difference in the distribution of hydrophobic residues between NHE1- and CNA peptides (Figure 3D and E). Such local structural differences between CHP2 and CNB, together with differences between target peptide sequences, may explain the selectivity of CHP1/2 toward the NHE members and of CNB toward CNA, and led us to predict that NHE1 may not be a target for CNB. In fact, we observed that GFP-tagged CNB was not localized to the plasma membrane when co-expressed with NHE1 (Figure 5C). On the other hand, since the C-lobe of KChIP1 is occupied by the α10 helix of itself (Figure 3C), KChIP1 associates with its target K^+-channel molecule only through the N-lobe (Zhou *et al*, 2004). Crystal structures have been also solved for several other Ca^{2+}-binding proteins belonging to the NCS family: recoverin (Flaherty *et al*, 1993), NCS-1 (Bourne *et al*, 2001), neurocalcin (Vijay-Kumar and Kumar, 1999), AtCBL2 (Nagae *et al*, 2003), and CIB (Gentry *et al*, 2005). Although all these proteins have hydrophobic crevices that would interact with the target molecules, the sizes and shapes of these crevices are clearly different. In contrast to calmodulin, which is able to interact with a variety of proteins with broad specificity, target molecules for CNB and NCS family proteins appear to be limited. Structural differences in the hydrophobic cleft together with highly specific polar interactions would enable the diverse array of Ca^{2+} binding proteins belonging to these families to associate selectively and tightly with the target molecules.

Of note, the N-lobe of CHP2 associates tightly with the C-lobe within a large area (Figure 3A). The contact area between the two domains is 1066 $Å^2$, accounting for 16.6 and 15.2% of the total surface areas of the N- and C-lobes, respectively. Such interaction between the two lobes would result in the formation of a rigid cleft structure independent of the target peptide. In fact, the structure of the hydrophobic cleft of CHP2 is very similar to that of target-free CHP1 (Naoe *et al*, 2005). In addition, the N-lobe of CHP2 does not contain the methionine residue that was suggested to produce plasticity allowing fine-tuning toward various target molecules in calmodulin (Osawa *et al*, 1998). Therefore, NHE1-peptide would enter the preformed cleft, rather than the interaction being caused by a conformational change in the cleft. This target-independent rigid structure would allow the CHP-unique region to exert specific physiological functions, beyond a role as a connecting linker. This is in contrast to calmodulin the flexible liker region between the two domains of which is known to act as a hinge when it recognizes various target molecules (Zhang *et al*, 1995).

CHP1/2 is myristoylated and has two Ca^{2+} ions. However, these properties are different from those of other CNB and NCS family proteins. Mutation of CHP1 that prevents myristoylation has no apparent effect on plasma membrane expression or the exchange activity of NHE1. Therefore, myristoylation of CHP1/2 would not be required for the plasma membrane translocation of NHE1 or for the exchange activity (Pang *et al*, 2001, 2004), in contrast to KChIP1 (An *et al*, 2000). In addition, unlike recoverin, which undergoes the Ca^{2+}-myristoyl switch (Ames *et al*, 1997), the myristoyl moiety of CHP1/2 would always be exposed outside the core structure upon interaction with NHE1 and probably embedded in the plasma membrane. Thus, the physiological function of myristoylation is still unknown. On the other hand,

unlike many other Ca^{2+}-binding proteins, only EF3 and EF4 of CHP1/2 are able to coordinate Ca^{2+} ions. Removal of Ca^{2+} with a Ca^{2+}-chelator significantly reduced the interaction between NHE1 and CHP2 (Supplementary Figure 1) and a double mutation of EF3 and EF4 of CHP1 abolished the interaction with NHE1 (Pang *et al*, 2004). Furthermore, the Ca^{2+} affinity of CHP1 increases markedly (40-fold) upon interaction with NHE1 (Pang *et al*, 2004). These findings suggest that Ca^{2+}-binding sites and the hydrophobic cleft are structurally coupled, that is, the Ca^{2+}-bound conformation of EF-hands is required for the formation of the appropriate structure of the hydrophobic cleft for the interaction with NHE1. By analogy with calmodulin (Zhang *et al*, 1995), we consider that Ca^{2+} binding opens the hydrophobic pockets of EF-hands so that the residues of the C-lobe can fit into the hydrophobic cleft. However, such Ca^{2+}-induced conformational changes of CHP1/2 bound to NHE1 would not occur physiologically in cells, since the Ca^{2+} affinity for such a complex would be extremely high, that is, K_d for Ca^{2+} ($2 \sim 3$ nM) is much less than the physiological cytosolic Ca^{2+} concentration (0.1–1 μM) (Supplementary Figure 1 and see also Pang *et al*, 2004). Hence, we suggest that Ca^{2+} bound to EF-hands plays a structural role in stabilizing the hydrophobic cleft of CHP1/2. In the case of NHE1, Ca^{2+}-induced activation would take place on another Ca^{2+}-binding protein CaM, which binds to the middle of the cytoplasmic domain of NHE1 (Bertrand *et al*, 1994; Wakabayashi *et al*, 1994).

Implications for roles of CHP in NHE function

We demonstrated that Ile534 and Ile537 in NHE1 are critical residues for interaction with CHP2 (Figure 5). Mutations of these residues resulted in a disruption of NHE1 function, as characterized by a drastic reduction of the maximal exchange activity and a large acidic shift of the pH_i-dependence of exchange (Figure 6). This is consistent with our previous findings obtained by simultaneous mutation of four hydrophobic residues (Phe526, Leu527, Leu530 and Leu531) of NHE1, substituted with Gln or Arg (Pang *et al*, 2001, 2004). On the other hand, deletion of the CHP-unique region (Δ94–104) significantly reduced the physiological exchange activity by inducing an acidic shift of the pH_i-dependence of $^{22}Na^+$-uptake (Figure 6B) and inhibited the rate of $^{22}Na^+$ efflux (Figure 6D), while preserving the maximal activity at acidic pH_i (Figure 6B), suggesting that this region functions as an important segment controlling pH_i by interacting with NHE1. Based on these findings, we propose that CHP1/2 plays two important roles in the function of NHE1. First, CHP functions as an obligatory subunit, which activates almost non-functional NHE1 by tightly associating with its cytoplasmic domain via the hydrophobic cleft. This activation is characterized by increases in both V_{max} and the H^+-affinity. Secondly, CHP would participate in the delicate pH_i regulation of NHE1 through the CHP-unique region, which is involved in modulation of the H^+-affinity, but not V_{max}.

We predict that CHP may stabilize the structure of the juxtamembrane domain by inducing a stable α-helix, thereby preserving NHE1 in the functional conformation. Indeed, circular dichroism measurements indicated that the CHP-free, CHP-binding peptide has no secondary structure in aqueous solution (data not shown), although we do not exclude the possibility that this region is folded within the entire structure. On the other hand, the dominant-negative effect of Δ94–104 raises the interesting possibility that it may regulate the pH_i-sensing by interacting with some regions of NHE1. We observed that NHE1 and CHP2 crosslinked with each other through IL5 of NHE1 and the CHP-unique region (Supplementary Figure 5), suggesting that these regions in the two proteins are located in accessible positions beneath the membranes. Since, similar to Δ94–104 of CHP2, mutation of Arg440 in IL5 results in a large acidic shift of the pH_i-dependence of $^{22}Na^+$-uptake and efflux (Wakabayashi *et al*, 2003a, b), we consider that IL5 would be one of targets for the CHP-unique region. Although we do not have direct evidence, IL4 may be another target region because mutation of Arg327 in IL4 has also been reported to lead to a similar functional defect of NHE1 (Lacroix *et al*, 2004). Activation of $^{22}Na^+$ efflux by cytosolic acidification predicted the existence of an additional H^+-regulatory site(s) (Figure 6C and D; Aronson *et al*, 1982; Wakabayashi *et al*, 2003a). This phenomenon does not appear to be fully explained by the recent allosteric model, in which only H^+-transport sites are assumed to participate in the cooperative H^+-activation of NHE1 (Lacroix *et al*, 2004). We speculate that multiple charged residues in loops of NHE1, as well as in CHP1/2, may serve as 'pH-sensor' sites, which accept protons, although further investigation will be required to support this concept. The recently reported crystal structure of the bacterial Na^+/H^+ antiporter, NhaA, predicted that modification of charged residues provided by cytoplasmic loops may activate NhaA by exposing the cation transport site via reorientation of transmembrane helices (Hunte *et al*, 2005).

Finally, it should be noted that the relatively long juxtamembrane domain (aa 503–595) of NHE1 is essential for the physiological exchange activity (Ikeda *et al*, 1997; Wakabayashi *et al*, 1997), although we focused on the CHP-binding domain in the present study. Similar to the CHP-binding region, it is likely that the region covering aa 503–595 forms a stable structure by interacting with several accessory factors. Indeed, this region appears to be structurally unstable when expressed in *Escherichia coli* or in mammalian cells as a single polypeptide, as evidenced by its rapid degradation (unpublished observation), despite the fact that the whole cytoplasmic domain can be easily expressed in these cells. In addition, a previous study (Aharonovitz *et al*, 2000) indicated that positively charged clusters (aa 509–516 and aa 552–560 in human NHE1) interact with polyphosphoinosides (PIP_2). These regions were also reported to interact with ezrin, although interaction with ezrin is independent of the exchange activity (Denker *et al*, 2000; Baumgartner *et al*, 2004). Furthermore, we recently reported that a region (aa 560–580) of NHE1 may be involved in dimeric interactions (Hisamitsu *et al*, 2004). Such homotypic interactions may provide another way for stabilization of the structure, as deletion of aa 560–580 resulted in a marked reduction of exchange activity by inducing the acidic shift of pH_i-dependence (Hisamitsu *et al*, 2004). These findings raise the possibility that multiple homotypic and heterotypic interactions may induce stabilization of the juxtamembrane region and thereby form a substructure regulating the exchange activity. Clearly, CHP is an obligatory member in such regulatory machinery of NHE1.

In summary, we first determined the crystal structure of CHP2 complexed with its binding region in NHE1 and

clarified the mechanism by which CHP tightly and specifically associates with plasma membrane members of the NHE family. Structure-based mutagenesis revealed the physiological importance of CHP in pH_i regulation by NHE1. Most Ca^{2+}-binding proteins have long been recognized to function as Ca^{2+}-sensors or Ca^{2+}-buffers. In contrast to this general understanding, CHP does not appear to be a Ca^{2+}-sensor, but rather acts as a critical regulator of pH-sensing activity in the exchangers, presumably mediated by the CHP-unique region. The results of the present study cast new light on a unique function of CHP that was not reported in other canonical EF-hand Ca^{2+}-binding proteins.

Materials and methods

Protein expression and purification

The complex of human full-length CHP2 (aa 1–196) with its binding region (aa 503–545) in NHE1 was expressed and purified essentially as described previously (Pang *et al*, 2004; Ben Ammar *et al*, 2005).

Crystallization and data collection

Crystals of the complex CHP2/NHE1-peptide were grown using the sitting-drop vapor diffusion technique at 20°C. To obtain the best crystal quality, 1.5 µl of the protein complex solution containing 20 mM yttrium chloride was mixed with 1 µl of the reservoir solution containing 200 mM ammonium acetate, 100 mM Bis–Tris, pH 5.5, and 25% (w/v) PEG 3350 as described previously (Ben Ammar *et al*, 2005). Crystals were not obtained without adding yttrium chloride to the crystallization solution, suggesting that yttrium ion(s) were involved in crystal packing. Therefore, taking advantage of the yttrium ion(s) in the crystal, we collected multiple wavelength data sets around the absorption edge of the yttrium atom at SPring-8 beamline BL44B2. A high-resolution single-wavelength data set ($\lambda = 1$ Å) was collected at beamline BL41XU at SPring-8. The statistics of the data collection are summarized in Table I.

Structural determination and refinement

The structure of the CHP2/NHE1-peptide complex was determined by MAD phasing. The program SOLVE (Terwilliger and Berendzen, 1999) was used to determine two yttrium positions and the initial phases with a figure of merit of 0.43 at 3.1 Å resolution. The program RESOLVE (Terwilliger, 2000) improved the phases and produced the initial polyalanine model, which covered 65% of the residues of the CHP2/NHE1–peptide complex. The model was built with TURBO-FRODO and refined against the high resolution data set to 2.7 Å using CNS (Brunger *et al*, 1998), and subsequent rounds of model building and refinement produced the final structural model. The residues in the final model lie in 87.2% in the most favorable and 12.8% in the additionally allowed regions of the Ramachandran plot. Refinement statistics are summarized in Table I. Figures 2–4 were generated using PyMOL graphing software (http://www.pymol.org).

Construction of mammalian expression plasmids

The plasmid carrying the cDNA encoding NHE1 containing unique restriction sites cloned into the mammalian expression vector pECE was described previously (Wakabayashi *et al*, 1992). Construction of plasmids for various NHE1 or CHP2 mutants tagged with GFP or hemagglutinin (HA) epitope YPYDVPDYAS was carried out by a PCR-based strategy as described previously (Wakabayashi *et al*, 2000). PCR fragments were digested and cloned into the appropriate restriction sites of vectors pECE or pGEFP-N1 (Clontech, Palo Alto, CA) for NHE1 or CHP2, respectively.

Cell culture and plasmid transfection

The exchanger-deficient cell line PS120 (Pouyssegur *et al*, 1984) and corresponding transfectants were maintained in Dulbecco's modified Eagle's medium containing 25 mM $NaHCO_3$ and supplemented with 5% (v/v) fetal calf serum. All cDNA constructs were transfected into PS120 cells with Lipofectamine 2000 (Invitrogen), and stable clones for NHE1 and its mutant constructs were selected by repetitive H^+-killing selection procedures as described previously (Wakabayashi *et al*, 1992). GFP-tagged CHP2 variants were stably expressed in cells expressing various mutant NHE1 proteins and fluorescence images were taken under a confocal fluorescence microscope (BioRad).

Measurement of $^{22}Na^+$-uptake and $^{22}Na^+$-efflux activities

$^{22}Na^+$-uptake activity was measured by the K^+/nigericin pH_i clamp method as described previously (Ikeda *et al*, 1997). Data were simulated by fitting the values to the sigmoidal dose–response equation, rate of EIPA-sensitive $^{22}Na^+$-uptake $= V_{max}/(1 + 10^{(\log(pK - pH_i)^n)})$ (pK, pH_i giving half maximal $^{22}Na^+$ uptake; n, Hill coefficient), using the simulation program included in Graphpad Prizm (Microsoft Corp., Redmond, WA). $^{22}Na^+$ efflux was measured as described previously (Wakabayashi *et al*, 2003a). Briefly, serum-depleted cells in 24-well dishes were loaded with $^{22}Na^+$ by preincubating them for 30 min at 37°C in chloride/KCl medium containing 1 mM $^{22}NaCl$ (37 kBq/ml) and at the same time pH_i-clamped at 7.5 or 7.2 in presence of 5 µM nigericin. The radioactive solution was removed and $^{22}Na^+$ efflux was initiated by adding the nonradioactive medium. At the times indicated in figures, cells were rapidly washed four times with ice-cold PBS and the remaining ^{22}Na-radioactivity in the cells was counted.

Coordinates

Coordinates and structure factor amplitudes have been deposited in the Protein Data Bank with accession code 2BEC.

Supplementary data

Supplementary data are available at *The EMBO Journal* Online.

Acknowledgements

We thank the staff at beamline BL44B2 and BL41XU, SPring-8, for support with data collection, Dr Sugawara and Dr Miyano (RIKEN Harima Institute) for fruitful discussion, Dr Tomoe Y Nakamura for critical reading of manuscript, and Dr Tianxiang Pang for the initial participation in this study. This work was supported by Grant nano-001 for Research on Advanced Medical Technology from the Ministry of Health, Labor, and Welfare of Japan and Grant-in-Aid for Priority Areas 13142210 for Scientific Research from the Ministry of Education, Science, and Culture of Japan. YBA is a Japan Society for the Promotion of Science (JSPS) Postdoctoral Fellow.

References

Aharonovitz O, Zaun HC, Balla T, York JD, Orlowski J, Grinstein S (2000) Intracellular pH regulation by Na(+)/H(+) exchange requires phosphatidylinositol 4,5-bisphosphate. *J Cell Biol* **150:** 213–224

Ames JB, Ishima R, Tanaka T, Gordon JI, Stryer L, Ikura M (1997) Molecular mechanics of calcium-myristoyl switches. *Nature* **389:** 198–202

An WF, Bowlby MR, Betty M, Cao J, Ling HP, Mendoza G, Hinson JW, Mattsson KI, Strassle BW, Trimmer JS, Rhodes KJ (2000) Modulation of A-type potassium channels by a family of calcium sensors. *Nature* **403:** 553–556

Aronson PS, Nee J, Suhm MA (1982) Modifier role of internal H+ in activating the Na+-H+ exchanger in renal microvillus membrane vesicles. *Nature* **299:** 161–163

Barroso MR, Bernd KK, DeWitt ND, Chang A, Mills K, Sztul ES (1996) A novel Ca2+-binding protein, p22, is required for constitutive membrane traffic. *J Biol Chem* **271:** 10183–10187

Baumgartner M, Patel H, Barber DL (2004) Na(+)/H(+) exchanger NHE1 as plasma membrane scaffold in the assembly of signaling complexes. *Am J Physiol Cell Physiol* **287:** C844–C850

Ben Ammar Y, Takeda S, Sugawara M, Miyano M, Mori H, Wakabayashi S (2005) Crystallization and preliminary crystal-

lographic analysis of the human calcineurin homologous protein CHP2 bound to the cytoplasmic region of the Na+/H+ exchanger NHE1. *Acta Crystallograph Sect F* **61:** 956–958

Bertrand B, Wakabayashi S, Ikeda T, Pouyssegur J, Shigekawa M (1994) The Na+/H+ exchanger isoform 1 (NHE1) is a novel member of the calmodulin-binding proteins. Identification and characterization of calmodulin-binding sites. *J Biol Chem* **269:** 13703–13709

Bourne Y, Dannenberg J, Pollmann V, Marchot P, Pongs O (2001) Immunocytochemical localization and crystal structure of human frequenin (neuronal calcium sensor 1). *J Biol Chem* **276:** 11949–11955

Brunger AT, Adams PD, Clore GM, DeLano WL, Gros P, Grosse-Kunstleve RW, Jiang JS, Kuszewski J, Nilges M, Pannu NS, Read RJ, Rice LM, Simonson T, Warren GL (1998) Crystallography & NMR system: a new software suite for macromolecular structure determination. *Acta Crystallogr D* **54** (Part 5): 905–921

Counillon L, Pouyssegur J (2000) The expanding family of eucaryotic Na(+)/H(+) exchangers. *J Biol Chem* **275:** 1–4

Denker SP, Huang DC, Orlowski J, Furthmayr H, Barber DL (2000) Direct binding of the Na–H exchanger NHE1 to ERM proteins regulates the cortical cytoskeleton and cell shape independently of H(+) translocation. *Mol Cell* **6:** 1425–1436

Engelhardt S, Hein L, Keller U, Klambt K, Lohse MJ (2002) Inhibition of Na(+)-H(+) exchange prevents hypertrophy, fibrosis, and heart failure in beta(1)-adrenergic receptor transgenic mice. *Circ Res* **90:** 814–819

Flaherty KM, Zozulya S, Stryer L, McKay DB (1993) Three-dimensional structure of recoverin, a calcium sensor in vision. *Cell* **75:** 709–716

Gentry HR, Singer AU, Betts L, Yang C, Ferrara JD, Sondek J, Parise LV (2005) Structural and biochemical characterization of CIB1 delineates a new family of EF-hand-containing proteins. *J Biol Chem* **280:** 8407–8415

Gutierrez-Ford C, Levay K, Gomes AV, Perera EM, Som T, Kim YM, Benovic JL, Berkovitz GD, Slepak VZ (2003) Characterization of tescalcin, a novel EF-hand protein with a single Ca2+-binding site: metal-binding properties, localization in tissues and cells, and effect on calcineurin. *Biochemistry* **42:** 14553–14565

Hisamitsu T, Pang T, Shigekawa M, Wakabayashi S (2004) Dimeric interaction between the cytoplasmic domains of the Na+/H+ exchanger NHE1 revealed by symmetrical intermolecular cross-linking and selective co-immunoprecipitation. *Biochemistry* **43:** 11135–11143

Hunte C, Screpanti E, Venturi M, Rimon A, Padan E, Michel H (2005) Structure of a Na+/H+ antiporter and insights into mechanism of action and regulation by pH. *Nature* **435:** 1197–1202

Ikeda T, Schmitt B, Pouyssegur J, Wakabayashi S, Shigekawa M (1997) Identification of cytoplasmic subdomains that control pH-sensing of the Na+/H+ exchanger (NHE1): pH-maintenance, ATP-sensitive, and flexible loop domains. *J Biochem (Tokyo)* **121:** 295–303

Inoue H, Nakamura Y, Nagita M, Takai T, Masuda M, Nakamura N, Kanazawa H (2003) Calcineurin homologous protein isoform 2 (CHP2), Na+/H+ exchangers-binding protein, is expressed in intestinal epithelium. *Biol Pharm Bull* **26:** 148–155

Karmazyn M (2001) Role of sodium-hydrogen exchange in cardiac hypertrophy and heart failure: a novel and promising therapeutic target. *Basic Res Cardiol* **96:** 325–328

Kissinger CR, Parge HE, Knighton DR, Lewis CT, Pelletier LA, Tempczyk A, Kalish VJ, Tucker KD, Showalter RE, Moomaw EW, Gastinel LN, Habuka N, Chen X, Maldonado F, Barker JE, Bacquet R, Villafranca JE (1995) Crystal structures of human calcineurin and the human FKBP12-FK506-calcineurin complex. *Nature* **378:** 641–644

Lacroix J, Poet M, Maehrel C, Counillon L (2004) A mechanism for the activation of the Na/H exchanger NHE-1 by cytoplasmic acidification and mitogens. *EMBO Rep* **5:** 91–96

Lin X, Barber DL (1996) A calcineurin homologous protein inhibits GTPase-stimulated Na-H exchange. *Proc Natl Acad Sci USA* **93:** 12631–12636

Mailander J, Muller-Esterl W, Dedio J (2001) Human homolog of mouse tescalcin associates with Na(+)/H(+) exchanger type-1. *FEBS Lett* **507:** 331–335

Nagae M, Nozawa A, Koizumi N, Sano H, Hashimoto H, Sato M, Shimizu T (2003) The crystal structure of the novel calcium-binding protein AtCBL2 from *Arabidopsis thaliana*. *J Biol Chem* **278:** 42240–42246

Naoe Y, Arita K, Hashimoto H, Kanazawa H, Sato M, Shimizu T (2005) Structural characterization of calcineurin B homologous protein 1. *J Biol Chem* **280:** 32372–32378

Orlowski J, Grinstein S (2004) Diversity of the mammalian sodium/proton exchanger SLC9 gene family. *Pflugers Arch* **447:** 549–565

Osawa M, Swindells MB, Tanikawa J, Tanaka T, Mase T, Furuya T, Ikura M (1998) Solution structure of calmodulin-W-7 complex: the basis of diversity in molecular recognition. *J Mol Biol* **276:** 165–176

Pang T, Hisamitsu T, Mori H, Shigekawa M, Wakabayashi S (2004) Role of calcineurin B homologous protein in pH regulation by the Na+/H+ exchanger 1: tightly bound Ca2+ ions as important structural elements. *Biochemistry* **43:** 3628–3636

Pang T, Su X, Wakabayashi S, Shigekawa M (2001) Calcineurin homologous protein as an essential cofactor for Na+/H+ exchangers. *J Biol Chem* **276:** 17367–17372

Pang T, Wakabayashi S, Shigekawa M (2002) Expression of calcineurin B homologous protein 2 protects serum deprivation-induced cell death by serum-independent activation of Na+/H+ exchanger. *J Biol Chem* **277:** 43771–43777

Perera EM, Martin H, Seeherunvong T, Kos L, Hughes IA, Hawkins JR, Berkovitz GD (2001) Tescalcin, a novel gene encoding a putative EF-hand Ca(2+)-binding protein, Col9a3, and renin are expressed in the mouse testis during the early stages of gonadal differentiation. *Endocrinology* **142:** 455–463

Pouyssegur J, Sardet C, Franchi A, L'Allemain G, Paris S (1984) A specific mutation abolishing Na+/H+ antiport activity in hamster fibroblasts precludes growth at neutral and acidic pH. *Proc Natl Acad Sci USA* **81:** 4833–4837

Putney LK, Denker SP, Barber DL (2002) The changing face of the Na+/H+ exchanger, NHE1: structure, regulation, and cellular actions. *Annu Rev Pharmacol Toxicol* **42:** 527–552

Terwilliger TC (2000) Maximum-likelihood density modification. *Acta Crystallogr D* **56** (Part 8): 965–972

Terwilliger TC, Berendzen J (1999) Automated MAD and MIR structure solution. *Acta Crystallogr D* **55** (Part 4): 849–861

Vijay-Kumar S, Kumar VD (1999) Crystal structure of recombinant bovine neurocalcin. *Nat Struct Biol* **6:** 80–88

Wakabayashi S, Bertrand B, Ikeda T, Pouyssegur J, Shigekawa M (1994) Mutation of calmodulin-binding site renders the Na+/H+ exchanger (NHE1) highly H(+)-sensitive and Ca2+ regulation-defective. *J Biol Chem* **269:** 13710–13715

Wakabayashi S, Fafournoux P, Sardet C, Pouyssegur J (1992) The Na+/H+ antiporter cytoplasmic domain mediates growth factor signals and controls 'H(+)-sensing'. *Proc Natl Acad Sci USA* **89:** 2424–2428

Wakabayashi S, Hisamitsu T, Pang T, Shigekawa M (2003a) Kinetic dissection of two distinct proton binding sites in Na+/H+ exchangers by measurement of reverse mode reaction. *J Biol Chem* **278:** 43580–43585

Wakabayashi S, Hisamitsu T, Pang T, Shigekawa M (2003b) Mutations of Arg440 and Gly455/Gly456 oppositely change pH sensing of Na+/H+ exchanger 1. *J Biol Chem* **278:** 11828–11835

Wakabayashi S, Pang T, Su X, Shigekawa M (2000) A novel topology model of the human Na(+)/H(+) exchanger isoform 1. *J Biol Chem* **275:** 7942–7949

Wakabayashi S, Shigekawa M, Pouyssegur J (1997) Molecular physiology of vertebrate Na+/H+ exchangers. *Physiol Rev* **77:** 51–74

Zachos NC, Tse M, Donowitz M (2005) Molecular physiology of intestinal Na+/H+ exchange. *Annu Rev Physiol* **67:** 411–443

Zhang M, Tanaka T, Ikura M (1995) Calcium-induced conformational transition revealed by the solution structure of apo calmodulin. *Nat Struct Biol* **2:** 758–767

Zhou W, Qian Y, Kunjilwar K, Pfaffinger PJ, Choe S (2004) Structural insights into the functional interaction of KChIP1 with Shal-type K(+) channels. *Neuron* **41:** 573–586

Available online at www.sciencedirect.com
SCIENCE DIRECT
Life Sciences 78 (2006) 882 – 887
Life Sciences
www.elsevier.com/locate/lifescie

Vagal stimulation suppresses ischemia-induced myocardial interstitial norepinephrine release

Toru Kawada [a,*], Toji Yamazaki [b], Tsuyoshi Akiyama [b], Meihua Li [a], Hideto Ariumi [a], Hidezo Mori [b], Kenji Sunagawa [c], Masaru Sugimachi [a]

[a] *Department of Cardiovascular Dynamics, Advanced Medical Engineering Center, National Cardiovascular Center Research Institute, 5-7-1 Fujishirodai, Suita, Osaka 565-8565, Japan*
[b] *Department of Cardiac Physiology, National Cardiovascular Center Research Institute, Osaka 565-8565, Japan*
[c] *Department of Cardiovascular Medicine, Graduate School of Medical Sciences, Kyushu University, Fukuoka 812-8582, Japan*

Received 30 November 2004; accepted 31 May 2005

Abstract

Although electrical vagal stimulation exerts beneficial effects on the ischemic heart such as an antiarrhythmic effect, whether it modulates norepinephrine (NE) and acetylcholine (ACh) releases in the ischemic myocardium remains unknown. To clarify the neural modulation in the ischemic region during vagal stimulation, we examined ischemia-induced NE and ACh releases in anesthetized and vagotomized cats. In a control group (VX, $n=8$), occlusion of the left anterior descending coronary artery increased myocardial interstitial NE level from 0.46 ± 0.09 to 83.2 ± 17.6 nM at 30–45 min of ischemia (mean ± SE). Vagal stimulation at 5 Hz (VS, $n=8$) decreased heart rate by approximately 80 beats/min during the ischemic period and suppressed the NE release to 24.4 ± 10.6 nM ($P<0.05$ from the VX group). Fixed-rate ventricular pacing (VSP, $n=8$) abolished this vagally mediated suppression of ischemia-induced NE release. The vagal stimulation augmented ischemia-induced ACh release at 0–15 min of ischemia (VX: 11.1 ± 2.1 vs. VS: 20.7 ± 3.9 nM, $P<0.05$). In the VSP group, the ACh release was not augmented. In conclusion, vagal stimulation suppressed the ischemia-induced NE release and augmented the initial increase in the ACh level. These modulations of NE and ACh levels in the ischemic myocardium may contribute to the beneficial effects of vagal stimulation on the heart during acute myocardial ischemia.

Keywords: Acetylcholine; Coronary occlusion; Ventricular pacing

Introduction

Acute myocardial ischemia disrupts normal neural regulation of the heart (Armour, 1999). During prolonged ischemia, myocardial interstitial norepinephrine (NE) and acetylcholine (ACh) levels are increased in the ischemic region via local releasing mechanisms independent of efferent autonomic activities (Schömig et al., 1987; Lameris et al., 2000; Kawada et al., 2000, 2001). The excess NE release is thought to aggravate ischemic injury to the myocardium (Schömig et al., 1987). On the other hand, vagal stimulation exerts antiarrhythmic effects in the early phase of acute myocardial ischemia (Rosenshtraukh et al., 1994; Vanoli et al., 1991). A recent study from our laboratory demonstrated that vagal stimulation improved the survival rate of chronic heart failure after myocardial infarction in rats (Li et al., 2004), suggesting a long-term ameliorative effect of direct neural interventions against certain heart diseases.

With respect to electrical stimulation of the vagus, whether it alters myocardial interstitial NE and ACh levels in the ischemic region during acute myocardial ischemia remains unknown. To test the hypothesis that vagal stimulation increases the ACh level and suppresses the NE level in the ischemic region, we measured myocardial interstitial NE and ACh levels during acute myocardial ischemia in anesthetized cats using a cardiac microdialysis technique (Akiyama et al., 1991, 1994; Yamazaki et al., 1997). Effects of vagal stimulation were examined with or without fixed-rate ventricular pacing.

* Corresponding author. Tel.: +81 6 6833 5012x2427; fax: +81 6 6835 5403.
E-mail address: torukawa@res.ncvc.go.jp (T. Kawada).

0024-3205/$ - see front matter © 2005 Elsevier Inc. All rights reserved.
doi:10.1016/j.lfs.2005.05.087

Materials and methods

This investigation conforms with the *Guide for the Care and Use of Laboratory Animals* published by the US National Institutes of Health (NIH Publication No. 85-23, revised 1996).

Surgical preparation

Twenty-four adult cats weighing from 2.2 to 3.8 kg were anesthetized by an intraperitoneal injection of pentobarbital sodium (30–35 mg/kg) and ventilated mechanically with room air mixed with oxygen. The depth of anesthesia was maintained with a continuous intravenous infusion of pentobarbital sodium (1–2 mg kg^{-1} h^{-1}) through a catheter inserted from the right femoral vein to the inferior vena cava. Systemic arterial pressure (AP) was monitored from a catheter inserted from the right femoral artery into the abdominal aorta. Heart rate (HR) was determined from an electrocardiogram using a cardiotachometer. Esophageal temperature of the animal was measured using a thermometer (CTM-303, TERUMO, Japan) and was maintained at around 37 °C using a heated pad and a lamp.

Bilateral vagal nerves were sectioned through a midline cervical incision. With the animal in the lateral position, the left fifth and sixth ribs were resected to expose the heart. A dialysis probe was implanted, using a fine guiding needle, into the anterolateral free wall of the left ventricle perfused by the left anterior descending coronary artery (LAD). A 3-0 silk suture was passed around the LAD just distal to the first diagonal branch for later coronary occlusion. When an experimental protocol required electrical stimulation of the vagal efferent nerves, bipolar platinum electrodes were attached to the cardiac end of sectioned vagal nerves bilaterally. The nerves and electrodes were covered with warmed mineral oil for insulation. When an experimental protocol required cardiac pacing, bipolar stainless-steel wire electrodes were sutured at the left ventricular apex away from the implanted dialysis probe. Heparin sodium (100 U/kg) was administered intravenously to prevent blood coagulation.

In additional four anesthetized cats, the left ventricle was implanted with a dialysis probe and a pair of pacing electrodes to examine the effects of left ventricular pacing alone on the myocardial interstitial NE levels. The dialysis probe and pacing leads were placed in the same manner as described in the previous paragraph.

At the end of the experiment, the experimental animals were killed with an overdose of pentobarbital sodium. Postmortem examination confirmed that the dialysis probe had been implanted within the left ventricular myocardium.

Dialysis technique

The materials and properties of the dialysis probe have been previously described (Akiyama et al., 1991, 1994). Briefly, we designed a transverse dialysis probe. A dialysis fiber (13 mm length, 310 μm O.D., 200 μm I.D.; PAN-1200, 50,000 molecular weight cutoff, Asahi Chemical, Japan) was glued at both ends to polyethylene tubes (25 cm length, 500 μm O.D., 200 μm I.D.). The dialysis probe was perfused at a rate of 2 μl/min with Ringer solution containing the cholinesterase inhibitor eserine (100 μM). Dialysate sampling was initiated 2 h after implanting the dialysis probe, when the dialysate concentrations of NE and ACh had reached steady states (Akiyama et al., 1991, 1994). The actual dialysate sampling lagged behind a given collection period by 5 min taking into account the dead space volume between the dialysis membrane and the sample tube. Dialysate concentrations of NE and ACh were measured separately by high performance liquid chromatography with electrochemical detection (DTA-300, Eicom, Japan). Details of the NE and ACh measurements have been previously described (Akiyama et al., 1991, 1994).

Protocols

Protocol 1 (VX, n = 8)

As a control experiment, we measured ischemia-induced NE and ACh releases during 60-min LAD occlusion in vagotomized animals. After collecting a 15-min baseline dialysate sample, we occluded the LAD for 60 min and collected four consecutive 15-min dialysate samples during acute myocardial ischemia. We then loosened the LAD snare and collected a 15-min dialysate sample during reperfusion.

Protocol 2 (VS, n = 8)

We examined the effects of vagal stimulation on ischemia-induced NE and ACh releases. To avoid possible preconditioning mimetic effects of ACh released by vagal stimulation (Przyklenk and Kloner, 1995; Kawada et al., 2002a), we initiated the bilateral vagal stimulation (5 Hz, 1 ms in pulse duration and 10 V in pulse amplitude) at the onset of LAD occlusion. The vagal stimulation continued for the 60-min ischemic period and the 15-min reperfusion period.

Protocol 3 (VSP, n = 8)

To eliminate the effects of bradycardia associated with vagal stimulation, we performed vagal stimulation under fixed-rate pacing conditions. We initiated the bilateral vagal stimulation (5 Hz, 1 ms in pulse duration and 10 V in pulse amplitude) and paced the heart from the onset of LAD occlusion to the conclusion of the experimental period. The ventricular pacing rate was set close to the HR recorded immediately before the LAD occlusion.

Supplemental protocol (n = 4)

To examine the effects of left ventricular pacing on the myocardial interstitial NE levels, we collected 15-min dialysate samples under control conditions as well as under left ventricular pacing at 170 beats/min.

Statistical analysis

All data are presented as means ± SE values. In each group, the effects of LAD occlusion on dialysate concentrations of NE and ACh were examined using a repeated-measures analysis of

variance followed by a Dunnett test against respective baseline concentrations. Because the variance of NE data was very large and increased with mean, the NE data were compared after the logarithmic transform (Snedecor and Cochran, 1989). Differences were considered significant at $P<0.05$. To examine the effects of vagal stimulation with or without the ventricular pacing, dialysate concentrations of NE and ACh were compared among the three groups at each corresponding time period using one-way analysis of variance followed by a Student–Newman–Keuls test for all pairwise comparisons (Glantz, 2002). The NE data were compared after the logarithmic transform. Differences were considered significant at $P<0.05$. Heart rate and mean AP were determined immediately before the coronary occlusion (designated as time 0), after 5, 10, 15, 30, 45, and 60 min of the occlusion, and after 15 min of reperfusion. One-way analysis of variance followed by a Student–Newman–Keuls test was also applied to compare HR and mean AP among the three groups at each time point.

Results

Fig. 1 depicts LAD occlusion-induced myocardial interstitial NE accumulation within the ischemic zone. The inset shows the NE levels during baseline conditions in a magnified ordinate. In the VX group, LAD occlusion increased the NE level approximately 200 fold compared to the baseline level at 45–60 min. This occlusion-induced NE accumulation was significantly suppressed in the VS group compared with the VX group in 15–30, 30–45, and 45–60 min time periods. The difference between the VS and VX groups did not reach statistical significance at the reperfusion period. In the VSP group, in which HR was kept constant, vagal stimulation did not attenuate the occlusion-induced NE accumulation. In the supplemental protocol, the baseline myocardial interstitial NE level was 0.17±0.01 nM. The NE level during ventricular pacing at 170 beats/min was 0.21±0.09 nM.

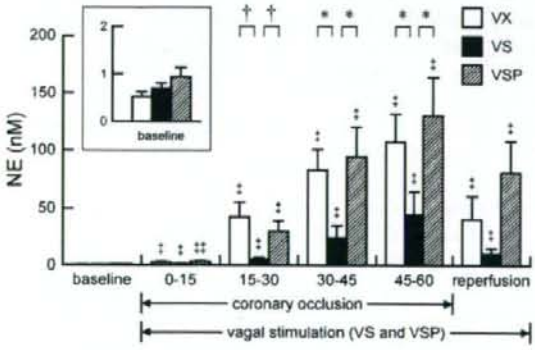

Fig. 1. Coronary occlusion-induced norepinephrine (NE) accumulation in the ischemic myocardium. VX: vagotomy, VS: vagal stimulation, VSP: vagal stimulation with ventricular pacing. The inset shows the baseline conditions with a magnified ordinate. Data are means±SE. ‡$P<0.01$ and ‡‡$P<0.05$ from the corresponding baseline value in each group. †$P<0.01$ and *$P<0.05$ by all pairwise comparisons among the three groups.

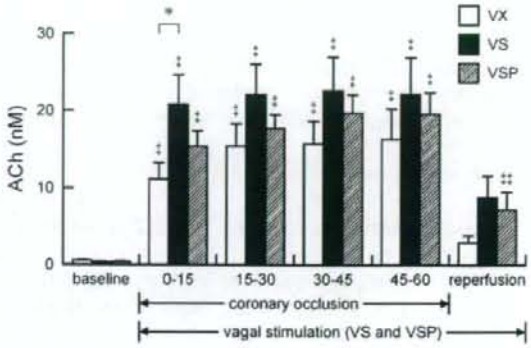

Fig. 2. Coronary occlusion-induced acetylcholine (ACh) accumulation in the ischemic myocardium. Data are means±SE. ‡$P<0.01$ and ‡‡$P<0.05$ from the corresponding baseline value in each group. *$P<0.05$ by all pairwise comparisons among the three groups.

Fig. 2 shows LAD occlusion-induced myocardial interstitial ACh accumulation within the ischemic zone. In the VX group, LAD occlusion increased the ACh level approximately 20 times higher than the baseline level at 45–60 min. The ACh level at 0–15 min was significantly higher in the VS than the VX group. For the rest of the ischemic period and reperfusion period, the differences between the VS and VX groups were not significant. The ACh levels in the VSP group did not differ from the VX group for any of the sampling periods.

Fig. 3 summarizes changes in HR and mean AP. In the VS group, HR was decreased by approximately 80 beats/min compared with the VX group at 5 min of coronary occlusion. The HR decrease continued for the rest of the ischemic period and reperfusion period. In the VSP group, HR was kept close to the preocclusion level, and it did not differ from the VX group

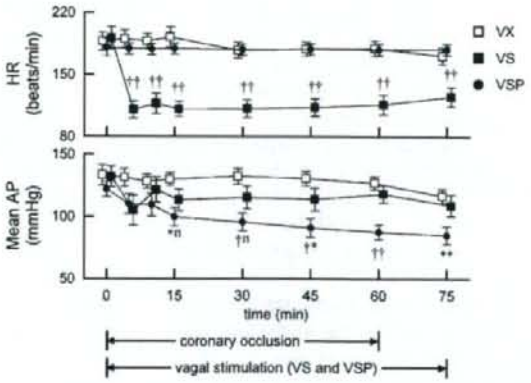

Fig. 3. Time courses of heart rate (HR) and mean arterial pressure (AP) during 60-min ischemia and 15-min reperfusion. The baseline values obtained just before coronary occlusion are plotted at time 0. Data points for VX and VSP groups are slightly displaced along the time axis for better view of overlapping points. Data are means±SE. In the HR data, †† represents statistical significance of $P<0.01$ from both the VX and VSP groups by all pairwise comparisons. In the AP data, when two characters are added to the VSP data point, the first and second characters represent the statistical significance from VX and VS groups, respectively. *, †, and n designate $P<0.05$, $P<0.01$, and "not significant", respectively.